International Journal of Pharmaceutics 665 (2024) 124642

Contents lists available at ScienceDirect

International Journal of Pharmaceutics

journal homepage: www.elsevier.com/locate/ijpharm

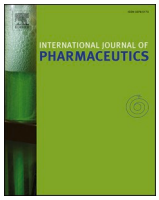

Transdermal delivery of bisphosphonates using dissolving and hydrogel-forming microarray patches: Potential for enhanced treatment of osteoporosis

Anastasia Ripolin [a], Fabiana Volpe-Zanutto [a,b], Akmal H. Sabri [a,1], Victor Augusto Benedicto dos Santos [c], Sidney R. Figueroba [c], Arthur A.C. Bezerra [c], Brendo Vinicius Rodrigues Louredo [d], Pablo Agustin Vargas [d], Mary B. McGuckin [a], Aaron R.J. Hutton [e], Eneko Larrañeta [a], Michelle Franz-Montan [c], Ryan F. Donnelly [a,*]

[a] School of Pharmacy, Queen's University Belfast, 97 Lisburn Road, Belfast BT9 7BL, UK
[b] Faculty of Pharmaceutical Sciences, R. Cândido Portinari, 200 - Cidade Universitária, Campinas - SP, 13083-871, Universidade Estadual de Campinas–UNICAMP, Brazil
[c] Department of Biosciences, Piracicaba Dental School, Universidade Estadual de Campinas–UNICAMP, Piracicaba, São Paulo, Brazil
[d] Department of Oral Diagnosis, Piracicaba Dental School, Universidade Estadual de Campinas–UNICAMP, Piracicaba, São Paulo, Brazil
[e] School of Pharmacy and Pharmaceutical Sciences, Ulster University, Cromore Road, Coleraine BT52 1SA, UK

ARTICLE INFO

Keywords:
Risedronate sodium
Alendronic acid
Dissolving microarray patches
Hydrogel-forming microarray patches
Transdermal
Osteoporosis

ABSTRACT

As of 2023, more than 200 million people worldwide are living with osteoporosis. Oral bisphosphonates (BPs) are the primary treatment but can cause gastrointestinal (GI) side effects, reducing patient compliance. Microarray (MAP) technology has the potential to overcome GI irritation by facilitating the transdermal delivery of BPs. This study examines the delivery of alendronic acid (ALN) and risedronate sodium (RDN) using dissolving and hydrogel-forming MAPs for osteoporosis treatment. In vivo testing on osteoporotic female Sprague Dawley rats demonstrated the efficacy of MAPs, showing significant improvements in mean serum and bone alkaline phosphatase levels, bone volume, and porosity compared to untreated bilateral ovariectomy (OVX) controls. Specifically, MAP treatment increased mean bone volume to 55.04 ± 2.25 % *versus* 47.16 ± 1.71 % in OVX controls and reduced porosity to 44.30 ± 2.97 % *versus* 52.84 ± 1.70 % in the distal epiphysis of the femur. In the distal metaphysis, bone volume increased to 43.32 ± 3.24 % in MAP-treated rats compared to 24.31 ± 3.21 % in OVX controls, while porosity decreased to 55.39 ± 5.81 % *versus* 75.69 ± 3.21 % in OVX controls. This proof-of-concept study indicates that MAP technology has the potential to be a novel, patient-friendly alternative for weekly osteoporosis management.

1. Introduction

Osteoporosis is the most common bone disease in humans, worldwide, representing a major public health problem. It is characterised by low bone mass and density and a disruption in bone microarchitecture, all of which result in a decrease in bone strength and subsequent increased risk of fractures (Porter and Varacallo, 2024; Sozen et al., 2017). Globally, osteoporosis causes more than 9 million fractures, according to latest figures, released in 2023. In the UK alone, over 3 million people are estimated to have osteoporosis with at least 500,000 fragility fractures reported to occur each year (NICE, 2019). The economic burden of osteoporosis fractures is significant, costing in and around $17.9 and £4 billion per year in the US and UK, respectively (Clynes et al., 2020).

Abbreviations: ALN, alendronic acid; ALP, alkaline phosphatase; BMD, Bone mineral density; BP, Bisphosphonate; D-MAP, dissolving microarray patch; EDS, Energy dispersive spectroscopy; GI, gastrointestinal, HF-MAP, hydrogel-forming microarray patch; MCT, microcomputed tomography; OVX, ovariectomy; PVA, poly (vinyl alcohol); PVP, poly(vinyl pyrrolidone); RDN, risedronate sodium, SEM, scanning electron microscopy.

* Corresponding author at: School of Pharmacy, Queen's University Belfast, Medical Biology Centre, 97 Lisburn Road, Belfast BT9 7BL, United Kingdom.
E-mail address: r.donnelly@qub.ac.uk (R.F. Donnelly).
[1] Present address: School of Pharmacy, University of Nottingham, University Park, Nottingham NG7 2RD, United Kingdom.

https://doi.org/10.1016/j.ijpharm.2024.124642
Received 10 June 2024; Received in revised form 23 August 2024; Accepted 24 August 2024
Available online 28 August 2024

Osteoporosis is often referred to as a 'silent disease' due to absence of symptoms, and is most commonly diagnosed when fractures occur due to disease severity (Cosman et al., 2014; de Oliveira et al., 2022). Post-menopausal osteoporosis develops as a result of decreased levels of oestrogen, directly affecting the bone remodelling process. Vitamin D and calcium deficiencies may also contribute to bone loss, as can long-term glucocorticoid treatment, or certain autoimmune diseases (Mirza and Canalis, 2015). The most commonly used diagnostic test for osteoporosis is bone densitometry, using a Dual Energy X-ray Absorptiometry (DEXA) scanner, outlined by the World Health Organisation (WHO) as the gold standard for bone mineral density measurements (Leslie *et al.*, 2006). Based on bone density measurements, management of the disease and associated bone loss, will primarily involve non-pharmacological, lifestyle changes, such as smoking cessation, reduced alcohol intake and healthy exercise. Pharmacological interventions involve the use of bisphosphonates (BPs), as first-line treatment agents, for all patients diagnosed with the disease. Alendronic acid (ALN) and risedronate sodium (RDN), specifically, are the two most commonly prescribed agents, at doses of either 10 mg and 5 mg daily, respectively, or, more commonly, 70 mg and 35 mg weekly. Alternatively, raloxifene, hormone replacement therapy or denosumab can be used (Zhu and March 2022). All of the above treatment options, ultimately work by reducing the rate of bone turnover (Drake *et al.*, 2008). Parathyroid hormones can be used as anabolic therapies which stimulate bone formation (NICE, 2019).

BPs exert their effects by inhibiting osteoclast activation and thus prevent bone resorption, ultimately slowing down bone loss, improving bone mineral density (BMD) and reducing a patient's risk of fractures (Zhu and March 2022). Interestingly, modification of the generic BP structure has significant effects on the potency and thus effective concentration of the drugs needed for antiresorptive activity. Potency may, in fact, be increased 10–10,000 fold in nitrogen-containing BPs, such as RDN and ALN, relative to the non-nitrogen-containing ones (Coxon et al., 2005). BPs have also been reported to selective target sites of active resorption high metabolic activity, such as trabecular regions of diseased bone tissue. Their distribution across the skeleton is thus varied.

All oral BPs have been reported as having low and variable bioavailabilities, due to their hydrophilic nature. Co-administration of the compounds with calcium or magnesium-containing foods may further hinder their intestinal absorption. Depending on the BP used, concentration and pH values, plasma and serum protein-binding may vary from 5-90 %. Gastrointestinal (GI) adverse effects are the most commonly reported reason for patient intolerance or non-compliance to oral BP treatments. Patients are counselled on administration of oral preparations, highlighting the importance of taking the dose on an empty stomach, with a full glass of water and standing or sitting upright for at least 30 min' post dose (NICE, 2019). Other side-effects associated with BP use are: osteonecrosis of the jaw (ONJ), atrial fibrillation, atypical femoral fractures, hypocalcaemia and vitamin D deficiency.

Most commonly prescribed marketed oral preparations of BPs, are thus commonly linked to oesophageal irritation, and ulceration, as discussed above. The mechanism by which bisphosphonates cause gastric damage, however, has not fully been established, with a variety of different explanations reported in the literature (Lichtenberger et al., 2000). It has been suggested that BPs may replace hydrophobic, acid-resistant phospholipids found on the gastric mucosal barrier, due to structural similarities. The weakening of this barrier therefore causes erosions and ulceration to the oesophagus, which may lead to undesired complications if left undetected (Peter et al., 1998; Vestergaard et al., 2010; Yamamoto et al., 2019). Intravenous (IV) preparations may cause flu-like symptoms as well as pain and inflammation at the site of action. Transdermal delivery of BPs, is an attractive alternative to the oral and IV routes, but has only recently been investigated for the delivery of RDN and ALN, either via transdermal gels, or with the aid of microneedle (MN) technology (Gyanewali et al., 2021; Katsumi et al., 2017; Kusamori et al., 2010; Naito et al., 2019).

MN technology involves the use of micron-scale needle projections, which, when inserted into the skin, penetrate through its outermost layers, creating microconduits for enhanced permeation of a variety of different compounds (Alkilani et al., 2015; Donnelly et al., 2012; Ramadon et al., 2021). MNs are pain-free and overcome issues relating to needle phobia. Multiple MNs are usually attached to a baseplate, forming a microarray patch (MAP), offering a more supportive platform for application to the skin. There are five different types of MNs, namely, solid, coated, hollow, dissolving and hydrogel-forming (Alkilani et al., 2015; Tuan-Mahmood et al., 2013). Dissolving MAPs (D-MAPs) consist of aqueous blends of biocompatible polymers loaded with the active drug. Upon application to the skin surface, the polymers dissolve, delivering the drug into the dermal region of skin for uptake by the microcirculation (Ramadon et al., 2021). Hydrogel-forming MAPs (HF-MAPs) consist of a drug-free, crosslinked hydrogel network as the MAP, which upon contact with interstitial fluid in the outer layers of skin, starts to swell, creating pores for controlled drug diffusion and permeation (Donnelly et al., 2012). The drug is incorporated into a separate reservoir layer, placed on top of the array, which dissolves, as MNs start to swell, thus allowing drug molecules to move through the swollen network and into the skin. Both MAP types are good candidates for self-administration and cannot be reused, so eliminate the risk of transmission of blood borne diseases. Additionally, HF-MAPs have the ability to control or sustain the release of compounds, by modifying polymer composition and/or the degree of crosslinking, to alter swelling kinetics and thus rates of diffusion and permeation (Garland et al., 2011).

Katsumi et al. (2012), investigated the use of D-MAPs for the transdermal delivery of ALN, both *in vitro* and *in vivo*. Recently, Sultana et al. (2023) reported the use of D-MAPs for the delivery of RDN nanotransferosomes *in vitro*. To date, there have not been any reports of the use of HF-MAPs for the transdermal delivery of BPs.

The overall aim of the study was to assess the treatment efficacy of BPs, specifically RDN and ALN, delivered transdermally, using MN technology, for the management of osteoporosis, compared to oral control treatments. The use of HF-MAPs, in particular, for the transdermal delivery of BPs within this study, is investigated for the first time. To test this hypothesis, an *in vivo* pharmacodynamic study was designed, using an osteoporotic female Sprague Dawley rat model.

2. Materials and methods

2.1. Materials

Poly(vinyl alcohol) (PVA) 31–50 kDa, PVA 85–124 kDa, acetonitrile (ACN) (suitable for HPLC, gradient grade, ≥ 99.9 %), trehalose dihydrate, gelatin, poly(ethylene glycol) (PEG) 10,000, *O*- phthalaldehyde (OPA), *N*-acetylcysteine (NAC), formaldehyde solution 37 %, and sodium acetate were purchased from Sigma-Aldrich (Dorset, UK). Poly (vinyl pyrrolidone) (PVP) 58 kDa, marketed as Plasdone™ k29/32 was obtained from Ashland (Wilmington, DE, USA). Gantrez® S-97 was provided by Ashland (Worcestershire, UK). Anhydrous citric acid was purchased from BDH laboratory supplies (Poole, Dorset, England). RDN was purchased from Cangzhou Enke Pharma-tech Co., ltd. and ALN from Tokyo Chemical Industry UK ltd, Oxford, UK. For the neonatal porcine skin used *in vitro*, stillborn piglets were obtained from a local farm immediately after birth and excised skin was stored at − 20 °C until further use.

2.2. Analytical methods

2.2.1. Analytical methods to be used for drug content analysis and in vitro detection and quantification of RDN

Detection and quantification of RDN was carried out using reverse-phase HPLC coupled with a UV detector on an Agilent 1220 Infinity LC system (Agilent™ Technologies U.K Ltd, Stockport, Greater Manchester, U.K), with a Venusil™ AA column (100 Å pore size 5 μm, 250

mm x 4.6 mm) (Phenomenex Ltd., Cheshire, United Kingdom). The column temperature was maintained at 40 °C, with a mobile phase composition of ACN:0.01 M sodium acetate pH 6.5 (15:85) at a flow rate of 0.6 mL/min. The UV detection wavelength was set at 264 nm, with an injection volume of 40 µL and a run time of 6 min.

2.2.1.1. Analytical methods to be used or drug content analysis and in vitro detection and quantification of ALN. ALN was derivatised according to methods described previously by González-Vázquez et al. (2017). Briefly, ALN standards were reacted at 50 °C in a 1:1 ratio (500 µL) with the derivatising reagent consisting of *O*- phthalaldehyde (OPA), *N*-acetylcysteine (NAC) and 0.05 M borate buffer pH 9.3, for a total of 20 min. A fluorescent microplate reader (BMG Labtech Ltd., Aylesbury, Buckinghamshire, UK) was used to detect and quantify ALN set at 355 nm excitation and 460 nm emission (gain 500). All derivatised samples were quantified immediately post reaction completion and 'blank' samples containing possible surrounding matrix components, were also derivatised and quantified accordingly, so as to eliminate any potential interferences with ALN samples.

2.3. Formulation and characterisation of dissolving microarray patches (D-MAPs)

D-MAPs were prepared, by adding 2.5 % w/w of each drug, individually, to an aqueous polymer blend of 10 % w/w PVP (MW 58 kDa) and 15 % w/w PVA (MW 31–50 kDa). Gels were thoroughly mixed, to ensure homogeneity, before being placed in a centrifuge at 5000 rpm for 10 min, to remove bubbles. Approximately 0.35 g of this formulation was cast onto moulds, before centrifugation at 3500 rpm for 15 min. These were then allowed to dry under ambient lab conditions for 48 h, before carefully removing dried D-MAPs from moulds (Fig. 1.).

D-MAPs were visually inspected using a Leica EZ4 D digital light microscope, to assess homogeneity and structural integrity of each patch, but also amongst batches of D-MAPs. The mechanical strength and insertion characteristics of formulated D-MAPs were tested using a TA.XT2 Texture Analyser (Stable Microsystems, Haslemere, UK), according to methods described previously (Larrañeta et al., 2014). Briefly, D-MAPs were attached to the Texture Analyser probe and inserted into 8 layers of Parafilm M® (skin simulant), at a speed of 1.19 mm/s, and a force of 32 N, for a total 30 sec. Individual layers of Parafilm M® were visually inspected, under the light microscope for the number of holes created. Needle insertion efficiency was calculated according to **Equation (1).**

$$Insertionefficiency(\%) = \frac{No.ofholesinParafilmM}{NumberofMNsonarray} \times 100 \quad (1)$$

Needle height reduction (%) was also measured, post insertion of D-MAPs into the skin simulant, as an indicator of MN strength. MAPs were firstly visualised under the light microscope, and their height marked as H_0 (pre-compression). Their height post compression was then recorded as H_c. Needle height reduction was subsequently measured using **Equation (2).**

$$Needleheightreduction(\%) = \frac{(H_0 - H_c)}{H_c} \times 100 \quad (2)$$

Additionally, the dissolution time of drug-loaded D-MAPs was calculated by adding individual MAPs to 10 mL of either pre-warmed 0.01 M sodium acetate buffer solution, pH 5.5, in the case of RDN, or deionised water (37 °C±1°C) for ALN, and recording the time taken for them to dissolve. Average drug content of each array was also determined, by taking samples from these dissolution studies, diluting accordingly, and analysing them using analytical methods described in Section 2.2.

2.4. Formulation and characterisation of hydrogel-forming MAPs (HF-MAPs)

Two types of HF-MAPs were formulated and characterised, according to protocols published previously. Briefly, Gantrez® hydrogels, were composed of 20 % w/w Gantrez® S-97, and 7.5 % w/w PEG 10,000 in deionised water (Thakur *et al.*, 2009; Thakur *et al.*, 2010; Donnelly et al., 2012). PVA/PVP hydrogels were composed of PVA (MW 85–124 kDa, 87–89 % hydrolysed) 15 % w/w, PVP (MW 58 kDa) 10 % w/w, and anhydrous citric acid (1.5 % w/w) in deionised water (Tekko et al., 2020). Aqueous blends were thoroughly mixed to ensure homogeneity before being placed in the centrifuge at 3500 rpm for 15 min, to remove air bubbles for further use. Approximately 0.3 g of each formulation was cast onto moulds, before further centrifugation at 3500 rpm for 15 min. Moulds were then allowed to dry under ambient lab conditions for 48 h before crosslinking in a hot air oven at 80 °C for 24 h, in the case of Gantrez® hydrogels and 130℃ for 3 h in the case of PVA/PVP hydrogels (Donnelly et al., 2012; Tekko et al., 2020). Finally, side walls formed during MAP preparation, were removed using a heated scalpel (Fig. 2.).

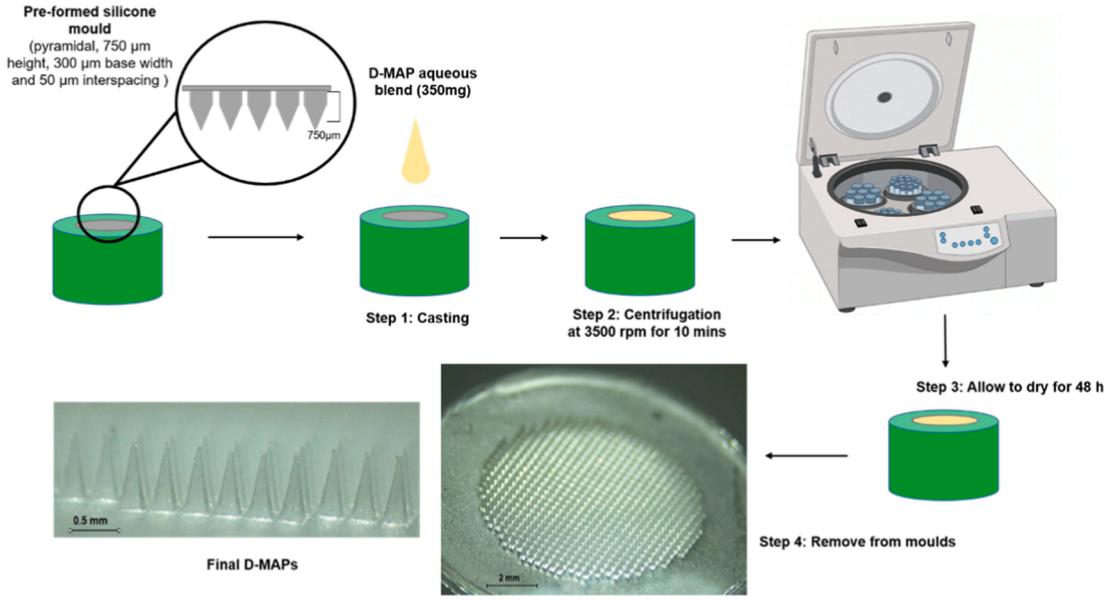

Fig. 1. Schematic representation of dissolving microarray patch (D-MAP) preparation protocol.

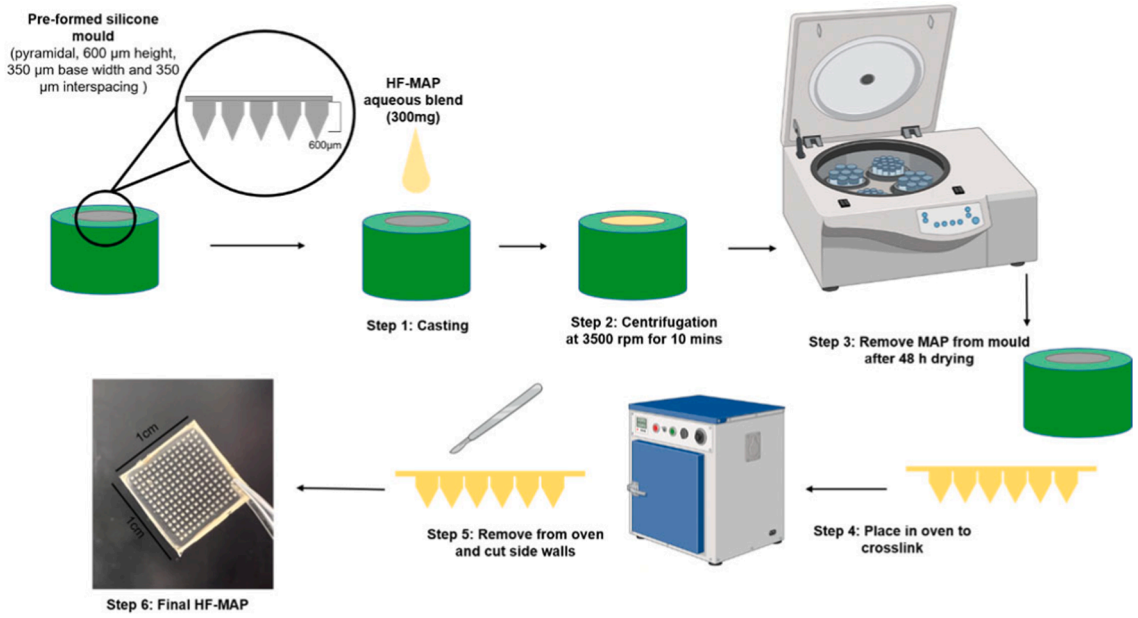

Fig. 2. Schematic representation of hydrogel-forming microarray (HF-MAP) preparation protocol.

The mechanical strength and insertion characteristics of formulated HF-MAPs were also tested using a TA.XT2 Texture Analyser, according to methods reported previously and also discussed in Section 2.3 (Larrañeta et al., 2014). Swelling profile of each hydrogel formulation was investigated, according to methods published previously (Donnelly et al., 2014b). Briefly, 1 cm^2 samples (1.0 x 1.0 cm) of each hydrogel formulation, were cut using a heated scalpel and calliper, and their dry weights recorded as M_0. Samples were then immersed in an excess of 0.01 M sodium acetate pH 5.5, and deionised water. Swollen hydrogels were removed at pre-determined time intervals, carefully dabbed with filter paper to remove excess surface liquid, and weighed (M_t). Percentage swelling of each film was calculated using **Equation (3).**, where M_0 is the initial mass of the 1 cm^2 hydrogel sample and M_t is the mass of the hydrogel at predetermined time points.

$$\%Swelling = \frac{(M_t - M_0)}{M_0} x100 \quad (3)$$

In addition to % swelling, the equilibrium water content (EWC) (%) and gel fraction (%) of each formulation, were determined. EWC represents the percentage of water that can be absorbed by the hydrogel at equilibrium (Sabri et al., 2022). Equilibrium was defined as the time point at which there were no marked changes in hydrogel mass (M_{eq}), in this case, 24 h (Anjani et al., 2021). EWC (%) was calculated according to **Equation (4)**, where M_0 is the initial mass of the 1 cm^2 hydrogel sample and M_{eq} is the mass of the hydrogel at equilibrium state.

$$EWC(\%) = \frac{(M_{eq} - M_0)}{M_{eq}} x100 \quad (4)$$

Gel fraction is used to assess crosslinking efficiency, or otherwise extent of crosslinking of each hydrogel formulation. At 24 h, swollen hydrogels were placed in an 80 °C oven for a further 24 h to dry, before determining their dried weight post swelling (M_d) (Sabri et al., 2022). Gel fraction (%) was calculated using **Equation (5).**, where M_0 is the initial mass of the 1 cm^2 hydrogel sample and M_d is the mass of the dried hydrogel after water extraction (Wong et al., 2015).

$$Gelfraction(\%) = \frac{M_d}{M_0} x100 \quad (5)$$

2.5. Formulation and characterisation of lyophilised wafer reservoirs (LYOs)

Briefly, LYO formulations contained 2.5 % w/w gelatin and 2.5 % w/w trehalose with 5 % w/w RDN and 2.5 % w/w ALN, separately, in deionised water. Formulations were sonicated for 30 min at 37 °C, to ensure complete dissolution and mixing, before casting into open-ended cylindrical moulds. Each formulation was frozen at −80 °C for 60 min and was then placed in a freeze dryer, for 26 h, according to protocols described previously (Donnelly et al., 2014b). Briefly, the lyophilisation process involved; primary drying for 90 min at a shelf temperature of −40 °C, 90 min at a shelf temperature of −30 °C, 90 min at a shelf temperature of −20 °C, 530 min at a shelf temperature of −10 °C and 90 min at a shelf temperature of 0–10 °C. The secondary drying phase was performed over 660 min at a shelf temperature of 25 °C and a vacuum pressure of 50 mTorr (Donnelly et al., 2014a).

LYOs were visually inspected under a Leica EZ4 D digital microscope and scanning electron microscope (SEM). Dissolution time and mean drug content of LYOs were determined, similarly to D-MAPs, following methods described in Section 2.3. LYO hardness was also determined using a Schleuniger 6D Tablet Hardness Tester (Schleuniger Pharmatron Inc., Oranmore Business Park, Galway, Ireland).

2.6. In vitro delivery of RDN and ALN from formulated MAPs

In vitro permeation studies were carried out using a Franz cell apparatus, with dermatomed neonatal porcine skin (average thickness 350 µm) as the skin membrane. Porcine skin was ethically obtained from stillborn piglets from a local farm, immediately after birth. Skin was cut to desired thickness using an electric dermatome (Integra Life SciencesTM, Padgett Instruments, NJ, USA) and was stored at −20 °C until further use. Prior to apparatus assembly, dermatomed porcine skin was fully thawed using phosphate buffered saline, and shaved, 30 min before set up. Skin was then attached to the donor compartment of each Franz cell, using cyanoacrylate adhesive. Following donor compartment assembly, both HF-MAP formulations were inserted into porcine skin, using manual pressure for 30 sec. D-MAPs were also inserted in the same manner. In the case of HF-MAPs, LYOs were placed on top of the HF-MAP with a quantity of 10 µL of dissolution media placed in between the two layers, to attach the reservoir. A cylindrical stainless-steel weight (5.0 g) was placed on top of each MAP, to ensure they

remained in place throughout the experiment. The donor compartment was added to the receiver compartment, before being clamped to secure the two in place, and covered in Parafilm M®, to prevent liquid evaporation. Sampling arms were also sealed, to prevent any potential water loss through evaporation. To maintain sink conditions, the receiver compartment was filled with either deionised water, in the case of ALN or 0.01 M sodium acetate buffer, pH 5.5 for RDN, both pre-warmed, degassed and maintained at 37 °C±1°C. Samples (200 μL) were taken at pre-determined time intervals and replaced with fresh, pre-warmed media, to maintain the total volume and prevent the formation of air bubbles. Samples were diluted accordingly, and filtered before analysing by means of HPLC-UV (RDN) or fluorescence spectrophotometry (ALN) post-derivatisation, as detailed in Section 2.2.

2.7. *In vivo delivery of RDN and ALN from formulated MAPs*

In the present study, an osteoporotic Sprague Dawley rat model was used to assess the pharmacodynamic effect of BP-loaded MAPs formulated and investigated throughout this work. The ovariectomised rat model, specifically, was selected as the most suitable one for this study, as it is the pre-clinical model of choice, approved by the United States Food and Drug Administration (FDA) (Thompson et al., 1995). By 12 weeks of age, female Sprague-Dawley rats have been proven to have reached sexual maturity, and peak bone mass for femurs and tibiae, and would be the most common age at which the ovariectomised model would be developed (Sengupta et al., 2005). Fig. 3. presents a brief outline of the *in vivo* study timeline, from model development to tissue analysis at the end of the study.

2.7.1. *Ethical approval*

This study was approved by the Research & Ethics Committee on the Use of Animals at the Universidade Estadual de Campinas (UNICAMP), Brazil, under protocol no. 6153–1/2022. Experimentation was conducted according to the policy of CONCEA (Conselho Nacional de Controle de Experimentação Animal – National Council for the Control of Animal Experimentation), under MCTI (Ministério da Ciência e Tecnologia – Ministry of Science and Technology), responsible for overseeing and communicating regulations for animal studies in Brazil, with implementation of the principles of the 3Rs (replacement, reduction, and refinement) at all stages.

2.7.2. *Osteoporotic disease model development*

The disease model was developed following methods described and performed previously by Figueroba et al. (2021). Rats were randomly divided into two groups, either undergoing bilateral ovariectomy (OVX) (42 rats) or SHAM surgery (7 rats). Fasted rats were weighed and anaesthetised by intraperitoneal (IP) injection, using a mix of ketamine (90 mg/kg) and xylazine (10 mg/kg). Following confirmation of anaesthesia, the surgical incision area was shaved and disinfected. Briefly, for the 42 rats undergoing bilateral ovariectomy (OVX group), bilateral flanks were incised, ovarian bundles ligated, ovaries were removed, before suturing the fascia and skin with a 5/0 silk thread. The 7 SHAM surgery rats (healthy controls), underwent a simulated surgical procedure, without the removal of ovaries, and received postoperative analgesia with intramuscular (IM) pethidine chloride (2 mg/kg) (Figueroba et al., 2021). OVX surgery took 5–10 min per rat and post-operative wounds were healed within 10 days of the procedure. Rats were housed individually to prevent contamination or wound opening, for a week, and were monitored closely for any post-operative complications. Housing conditions were set at an average temperature of 23 °C, and a 12-hour light/12-hour dark artificial system with fluorescent lamps.

2.7.3. *Pharmacodynamic study design*

The study was conducted using female Sprague Dawley rats (n = 37 OVX rats, n = 5 healthy (SHAM) rats) aged 6 months at the time of treatment initiation and with a mean weight of 358.83 ± 26.6 g for OVX and 271.82 ± 15.5 g for SHAM. Rats were divided into eight cohorts, as illustrated in Table 1., also summarising dosing methods and total dose administered to rats. Oral solutions and MAPs were administered once a week for a total of 8 weeks.

'SHAM' rats in cohort (1) served as the healthy control group, while 'OVX control' rats cohort (2), served as the disease control with no treatment. Oral ALN and RDN groups, cohorts (3) and (4), served as reference treatment groups. These rats were treated with doses equivalent to established human doses of each BP, with proven therapeutic efficacy. Sample analysis from this group should therefore reflect intended treatment outcomes, for comparison with MAP cohorts. The remaining 4 cohorts received ALN and RDN *via* formulated MAPs, with HF-MAPs and LYOs applied to animals in cohorts (5) and (6), and D-MAPs applied to those in cohorts (7) and (8). MAP dosing was based on maximum drug loading into each formulation, to establish treatment

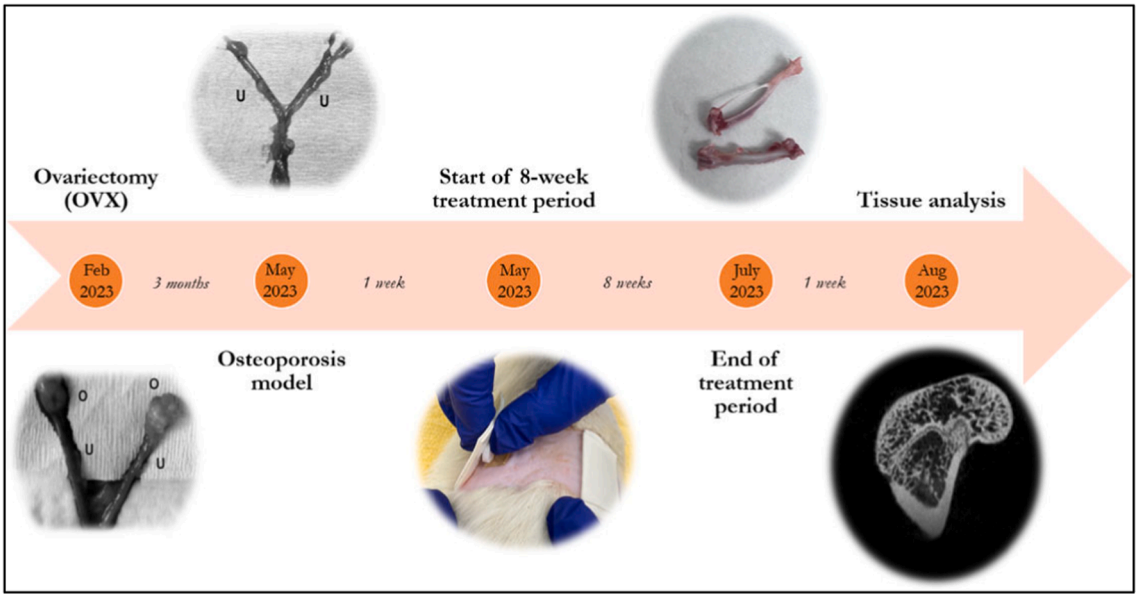

Fig. 3. In vivo pharmacodynamic study timeline from February to August 2023, carried out at Piracicaba Dental School, University of Campinas–UNICAMP.

Table 1
Details of doses administered to animals in each cohort.

Cohort	Number of animals	Dosing method	Total dose administered once weekly (mg/rat)
SHAM (1)	5	–	–
OVX control (2)	4	–	–
Oral ALN (3)	4	0.5 mL ALN solution (4.936 mg/mL)	2.47
Oral RDN (4)	4	0.5 mL RDN solution (2.468 mg/mL)	1.23
HF-ALN (5)	6	2 x HF-MAPs with ALN LYO	18.88
HF-RDN (6)	7	2 x HF-MAPs with RDN LYO	47.44
D-ALN (7)	6	4 x ALN D-MAPs	20.52
D-RDN (8)	6	4 x RDN D-MAPs	28.00

efficacy as part of the proof-of-concept setup. Higher doses were loaded into MAPs as opposed to oral gavages, to account for LYO leakage and incomplete dissolution of arrays in the skin.

2.7.4. Preparation of oral gavage for control rat cohorts

Oral doses for both drugs were calculated based on marketed human oral doses of both drugs, and by employing the 'Formula for Dose Translation based on body surface area' (Reagan-Shaw et al., 2008). Rats in oral control cohorts were to receive 0.5 mL of a solution containing either 2.468 mg/mL RDN or 4.936 mg/mL ALN. Briefly, raw drug powder was weighed out and made up to the appropriate volume using deionised water. Solutions were vortexed until fully homogenous and clear, and set aside for administration *via* oral gavage. Oral solutions were prepared freshly on the morning of administration.

2.7.5. Application of formulated MAPs to relevant rat cohorts

Rats in MAP treatment cohorts were appropriately sedated using gaseous anaesthesia (2–4 % isoflurane in oxygen), and the hair on their backs was shaved with electric clippers, followed by hair removal cream (Veet sensitive skin, Slough, UK). After a 24 h recovery period, MAPs were applied to clean, hair-less regions on the backs of the animals. Specifically, two HF-MAPs were applied to each rat in cohorts (5) and (6), whilst four D-MAPs were applied to the back of each rat in cohorts (7) and (8). MAPs were removed after 24 h.

2.7.6. Assessment of treatment efficacy

Weekly treatment with either oral solutions or formulated MAPs, continued for 8 weeks in total, before culling all rats using a mixture of ketamine (0.015 mL/kg) and xylazine (0.05 mL/kg) followed by cardiac puncture. Tissues of interest were removed, appropriately labelled and stored in 10 % neutral buffered formalin (NBF), pH 7.4, for further testing. Details of tissue samples collected and analysis schedules are summarised in Table 2.

Table 2
Details of tissue/sample collection after rat culling and intended analysis.

Tissue/Sample collection	Number collected	Type of analysis	Timeline of analysis
Rat serum	42 (all rats)	Rat ALP ELISA kit	2 days
Skin	18 (3 x cohorts 1, 2, 5–8)	Histological analysis	1 week
Femurs (R&L)	84 (all rats)	R- SEM/EDS analysis L- Micro-CT analysis	1.5 weeks 1 month
Tibiae (R)	42 (all rats)	R- Bone ALP ELISA	2 days

2.7.6.1. Serum and tissue collection, handling, processing and storage for analysis. Blood samples from cardiac punctures were placed in 2 mL Eppendorf tubes, appropriately labelled, and left to stand for 15–30 min, allowing the blood to clot. Following this, samples were placed in a centrifuge at 2,000 rpm for 10 min at 4 °C, and the resulting supernatant removed and placed in clean tubes. Serum samples were stored at −80 °C until further analysis. Skin samples were removed from all MAP cohorts (n = 3 per cohort), plus SHAM and OVX groups, placed on filter paper and carefully folded into plastic containers filled with 10 % NBF. Samples were stored at ambient temperature until further analysis. Both femurs and right tibiae of each of the 42 rats were removed, by separating bone from surrounding soft tissue and stored in 10 % NBF, at fridge temperature. Right tibiae used for alkaline phosphatase (ALP) estimation, were wrapped in damp gauze and placed in a −80 °C freezer until further analysis.

2.7.6.2. Alkaline phosphatase (ALP) measurements using an enzyme-linked immunosorbent assay (ELISA). Serum and bone alkaline phosphatase (ALP) levels were measured using an enzyme-linked immunosorbent assay (ELISA), purchased from ABclonal® UK ltd. (Port Talbot, UK). The ELISA employed a quantitative sandwich enzyme immunoassay technique, with rat ALP-specific antibodies pre-coated onto microplates. Serum samples were fully thawed for analysis and tibiae samples were homogenised using a Tris-HCl extraction buffer, with the aid of an Ultra-Turrax® homogeniser (IKA ltd, Staufen, Germany), before centrifuging to remove supernatant solutions for analysis. Analysis was carried out according to methods detailed in the ELISA kits, before determining optical density, using a microplate reader.

2.7.6.3. Scanning electron microscope (SEM) and energy dispersive X-ray spectroscopy (EDS) analysis of right femur. Right femur samples were visualised using scanning electron microscopy (SEM) but also subjected to Energy Dispersive Spectroscopy (EDS) (Noran Instruments Inc, Middleton, WI, USA), to determine calcium/phosphorus (Ca/P) ratios within each sample, using a JSM-5600LV Scanning electron microscope, (JEOL ltd, Tokyo, Japan). Femur samples were cleared of any remaining soft tissue on their outer surface and sliced down the middle and along the diaphysis, using a Model 650 Low speed diamond wheel saw (South Bay Technology ltd), before placing in an ascending ethanol series, to dehydrate samples. Bone samples were coated in carbon, using the Denton Vacuum Desk II apparatus (Denton Vacuum Mooreston, NJ, USA) for EDS analysis and in gold, using the Balzers Sputter Coater SCD 050, (Bal-Tec, Switzerland) for SEM imaging. EasyMicro® software was used to analyse the elemental composition of three distinct regions of the femur, illustrated in Fig. 4.

2.7.6.4. Microcomputed tomography (MicroCT/μCT) analysis of left femur. Left femurs were removed from the fridge and thoroughly dried before being placed into the SkyScan® 1172 X-ray microtomography machine (Aartselaar, Belgium), (X-ray source point size < 5 μm; camera pixel size of 21.03 μm). Bones were rotated 360 degrees in a 0.70-degree rotation pitch. X-ray configurations were standardised to 100 kV and 100 μA, with an exposure time of 0.2 sec per frame and averaging frames of 3. The scan time of each sample was 1 h producing 1123 contiguous layers with a nominal resolution of 3 μm. Images were reconstructed using Bruker™ 1.4.4.0 DataViewer and analysed using CTAn analyser 1.12.0.0 (SkyScan® softwares). Bones were analysed in terms of (%) bone volume/tissue volume (BV/TV), (%) porosity, trabecular number (Tb.N; 1/μm), trabecular separation (Tb.Sp; μm) and trabecular thickness (Tb.Th; μm), parameters commonly used to assess bone microarchitecture (Wu et al., 2015). Results of the analysis focused on the investigation of the distal epiphysis and metaphysis, in a sagittal plane, as depicted in Fig. 5.

2.7.6.5. Histological analysis of skin samples. Skin samples were

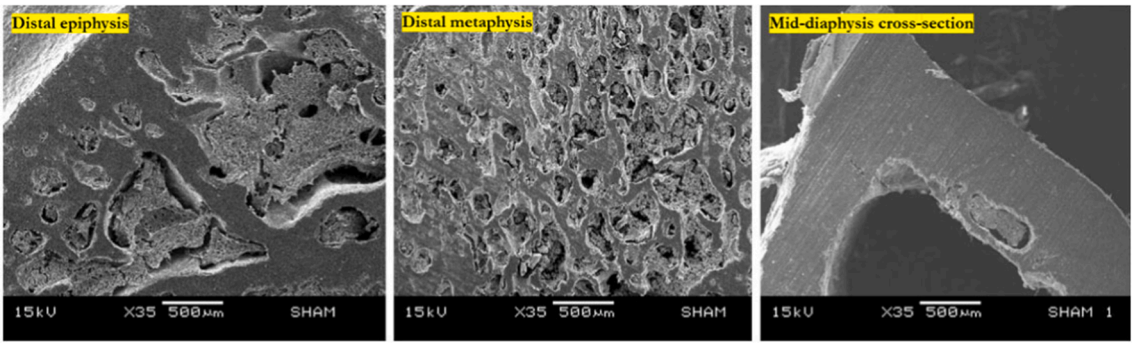

Fig. 4. Regions of interest for electron dispersive spectroscopy (EDS) analysis.

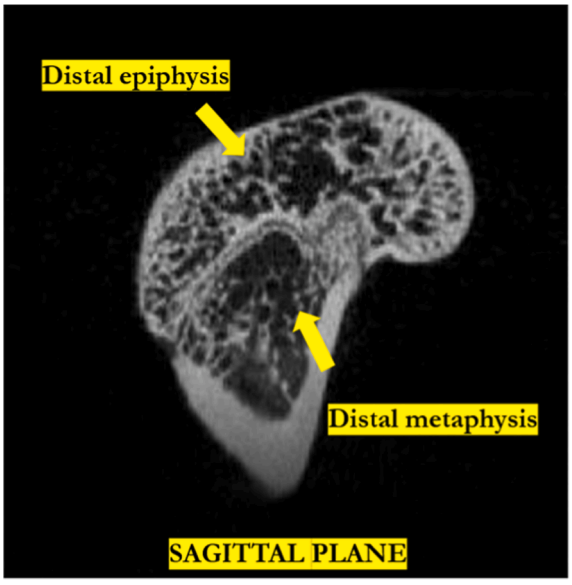

Fig. 5. Regions of interest for microcomputed tomography (MicroCT) analysis.

removed from 10 % NBF and patted dry with filter paper before slicing down areas of irritation. Tissue samples were placed in plastic tissue cassettes and subjected to an ascending ethanol series, to dehydrate, before embedding in liquid paraffin. Paraffin embedded sections of 4 µm thickness were cut from samples and stained with haematoxylin-eosin (H&E), using an LST™ 94 Linear Slide Stainer (Hestion Scientific PTY ltd., Australia) for subsequent microscopic analysis.

2.8. Statistical analysis

All data is expressed as means ± standard deviation (S.D.), unless otherwise stated in figure legends, and was processed using Microsoft Office 365®. GraphPad Prism® 9.2.0 (283) (GraphPad Software, San Diego, CA, USA) was used to statistically analyse data and produce graphical presentations. Statistical tests performed include parametric and non-parametric tests, such as t-tests, a one-way analysis of variance (ANOVA) and Mann-Whitney U, were appropriate, with a value of $p < 0.05$ denoting statistical significance. For *in vivo* data, due to the large amount of variables in the study design and small number of rats per cohort, in-depth and multiple comparison statistical analysis was not carried out.

3. Results and discussion

3.1. Analytical method validation

A simple, reliable HPLC-UV method was validated for the detection and quantification of RDN, according to ICH guidelines. This method had a linear range of 1.56–100 µg/mL, an LOD of 1.49 µg/ mL and LOQ of 4.52 µg/mL. At high (100 µg/mL), medium (25 µg/mL) and low (6.25 µg/mL) concentration points of the validated range, accuracy (95–105 % recovery) and precision (<5% coefficient of variance), fell within recommended guidelines. Similarly, a fluorescent microplate reader method was validated for the detection and quantification of ALN, post-derivatisation with OPA and NAC, with a linear range of 1.95–125 µg/mL, an LOD of 1.99 µg/mL and LOQ of 6.03 µg/mL. At high (125 µg/mL), medium (31.25 µg/mL) and low (7.8 µg/mL) concentration points of the validated range, accuracy (95–105 % recovery) and precision (<5% coefficient of variance), fell within recommended guidelines.

3.2. Formulation and characterisation of dissolving microarray patches (D-MAPs)

Both BPs were incorporated into D-MAPs and visually inspected under the light microscope (Fig. 6.), before subjecting to compression and insertion studies, as described in Section 2.3. The final D-MAPs produced, were composed of 600 needles arranged in a circular layout, perpendicular to the base and of pyramidal shape (approximately 750 µm in height, with base width of 300 µm, and 50 µm interspacing on a 0.7 cm^2 array). Both RDN and ALN D-MAPs inserted through to the 4th layer of Parafilm M®, equating to approximately 504 µm in depth. In terms of needle height reduction, post compression, RDN D-MAPs showed a mean 4.84 ± 3.57 % height reduction, whilst ALN D-MAPs showed a 5.52 ± 2.83 % reduction. Mean dissolution time for RDN D-MAPs was calculated at 10.5 ± 1.5 min, *versus* 11.5 ± 2.0 min for ALN D-MAPs. Average drug content of RDN D-MAPs was estimated at 7.0 ± 0.6 mg per patch, and 5.13 ± 0.23 mg for ALN ones.

3.3. Formulation and characterisation of hydrogel-forming patches (HF-MAPs)

Similar to D-MAPs, HF-MAPs were visualised under the light and scanning electron microscopes (Fig. 7.), before subjecting to compression and insertion studies. Final HF-MAPs produced were composed of 196 needles arranged in a 14 x 14 formation, perpendicular to the base and of pyramidal shape (approximately 600 µm in height, with base width of 350 µm, and 350 µm interspacing on a 1 cm^2 array). Both HF-MAP formulations inserted through to the 4th layer of Parafilm M®, with a mean needle height reduction for PVA/PVP hydrogels equal to 3.81 ± 1.51 %, *versus* 10.06 ± 1.25 % for Gantrez® hydrogels. Swelling characteristics of the two formulations were investigated by immersing them in 0.01 M sodium acetate pH 5.5 and deionised water, as the two

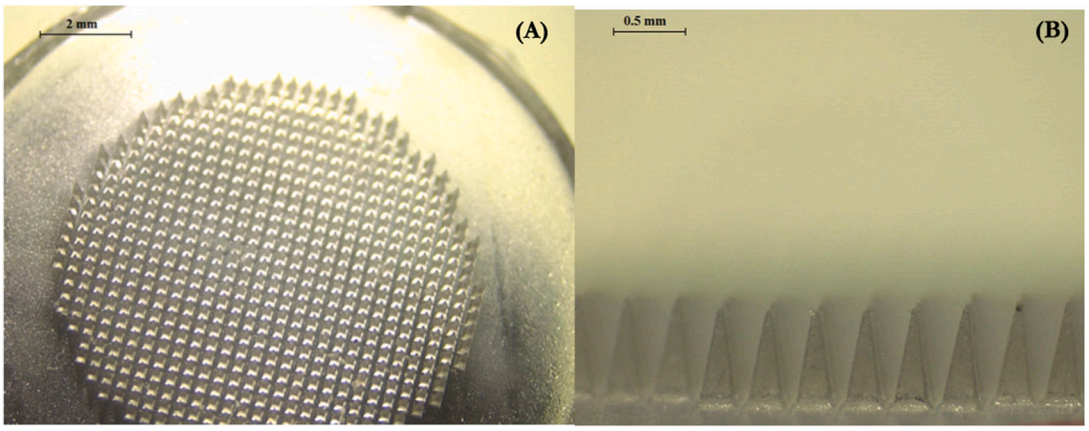

Fig. 6. Representative light microscope images of formulated dissolving microarray patches (D-MAPs) **(A)** and individual needles **(B)**.

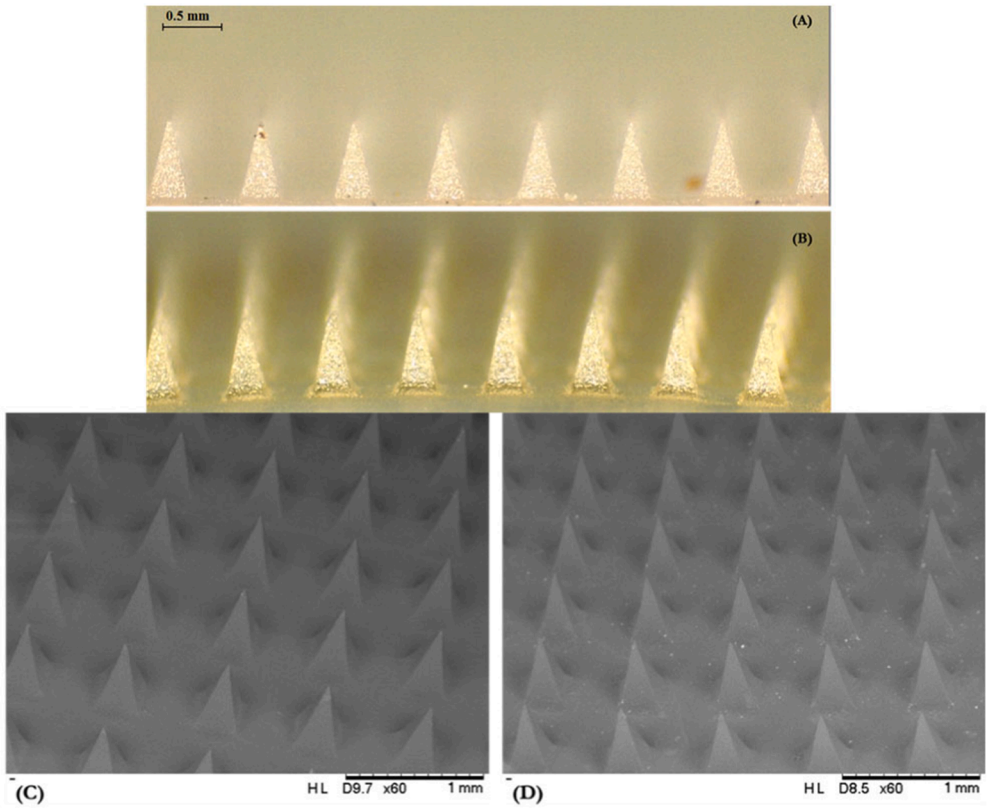

Fig. 7. Representative images of formulated Gantrez® **(A, C)** and PVA/PVP **(B, D)** hydrogel-forming microneedle arrays (HF-MAPs), obtained using the digital light and scanning electron microscopes.

mediums of interest. Fig. 8. shows the percentage swelling of each hydrogel formulation over 24 h, in the two mediums of interest, calculated according to **Equation (3).** Percentage swelling for each hydrogel did not significantly differ between the two liquid mediums. Upon statistical analysis of results, by means of a one-way ANOVA test, a significant difference in overall swelling capacity of PVA/PVP *versus* Gantrez® was seen ($p = 0.0094$). At the 24 h time point, an approximate 2.5-fold difference in % swelling was observed between the two hydrogels, in both mediums tested.

Gantrez® hydrogels showed a mean 1189.93 ± 52.84 % swelling in 0.01 M sodium acetate (pH 5.5) and 1280.75 ± 102.70 % in deionised water *versus* a significantly lower 470.67 ± 59.44 % and 496.27 ± 19.31 % for PVA/PVP in respective media. PVA/PVP hydrogels have been reported to swell less, over the course of 24 h, compared to Gantrez® hydrogels, owing to tighter crosslinks between polymeric monomers and the crosslinking agent, preventing excess liquid from entering (Tekko et al., 2020). In the hydrogel network of Gantrez®, PEG 10,000 acts as the crosslinker, but due to its inherent lower number of reactive hydroxyl- groups and larger size compared to citric acid, ester bond formation with carboxy- groups on Gantrez® monomers, lead to the formation of a more open, porous network, able to absorb and retain larger amounts of liquid, corresponding to higher % swelling (Donnelly et al., 2014a).

EWC and gel fraction were also calculated for each formulation, according to **Equations (4) and (5)**, and presented in Fig. 8**.** EWC (%) was recorded as 85 ± 1.7 % for PVA/PVP in sodium acetate buffer *versus* 94 ± 2.0 % for Gantrez® hydrogels and 84 ± 2.0 % for PVA/PVP in deionised water *versus* 87 ± 6.5 % for Gantrez®. As expected in both

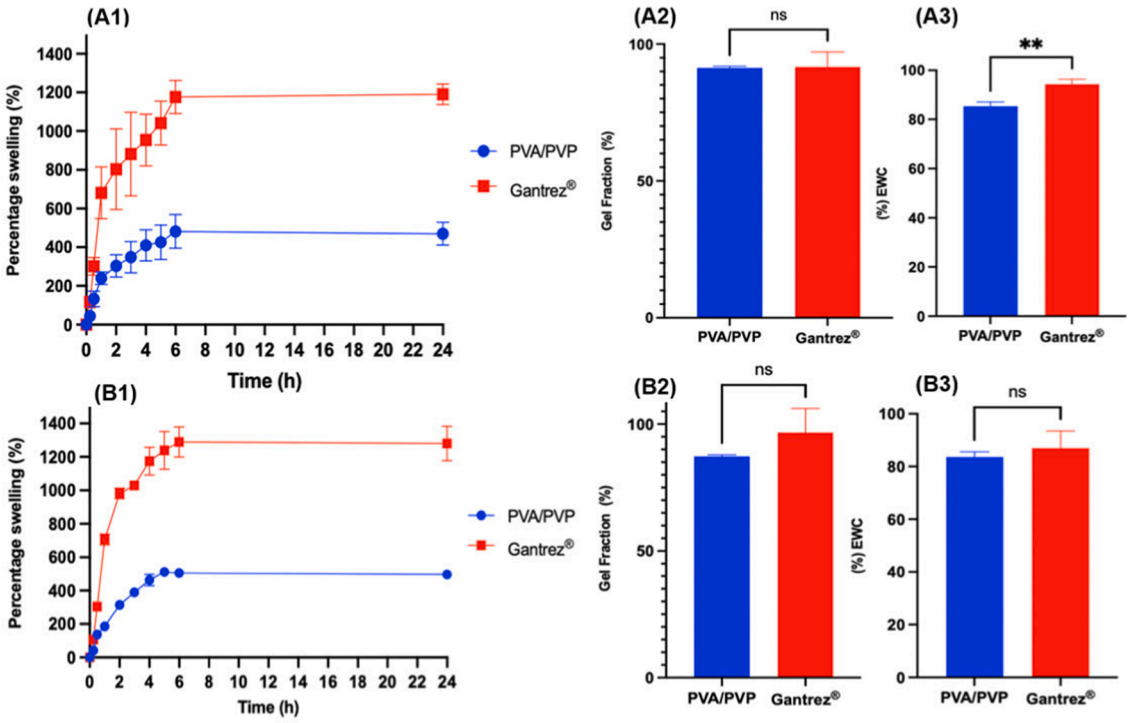

Fig. 8. **(A1-3)** Percentage swelling over 24 h, gel fraction (%) and equilibrium water content (%) of PVA/PVP and Gantrez® hydrogels in 0.01 M sodium acetate (pH 5.5) **(B1-3)** in deionised water; (Means ± S.D., n = 5).

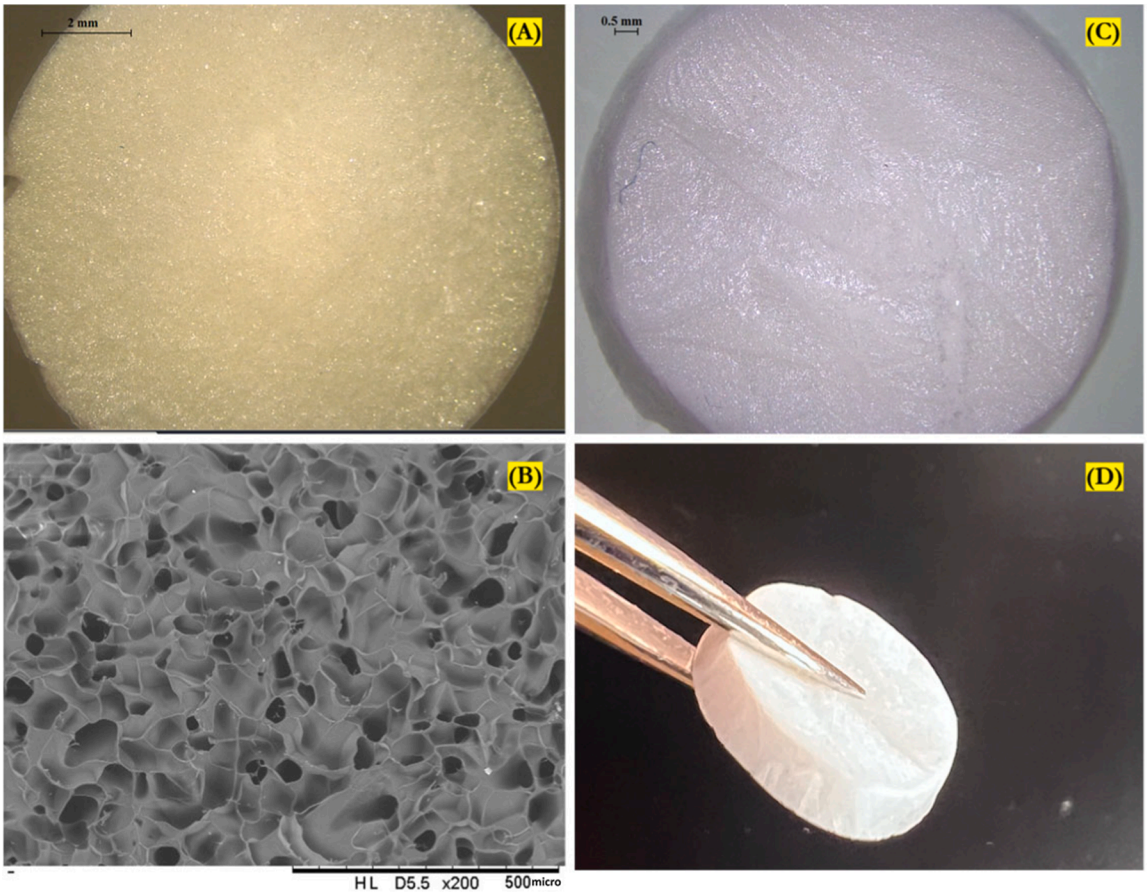

Fig. 9. Representative images of RDN lyophilised wafer reservoirs, visually inspected under the light and scanning electron microscopes **(A, B)** and ALN lyophilised wafer reservoirs **(C, D)**.

cases, Gantrez® hydrogels showed a higher % EWC, corresponding to their ability to absorb more liquid compared to PVA/PVP hydrogels, owing to the more porous structure, discussed previously (Anjani et al., 2021). Gel fraction was determined in both mediums of interest, and no significant differences between the two hydrogel formulations were observed. PVA/PVP hydrogels did have a slightly lower gel fraction, compared to Gantrez®, in line with literature reports, possibly due to a small proportion of polymer remaining unreacted within the matrix (Tekko et al., 2020). There is thus, a small amount of polymer, available for dissolution and entry into the skin upon application, however PVP is a biocompatible polymer, widely used within the industry and in the manufacture of MAPs specifically, and so, minimal amounts of polymer aren't expected to cause any safety concerns (Tekko et al., 2020).

3.4. Formulation and characterisation of lyophilised wafer reservoirs (LYOs)

LYOs containing each of the BPs, were formulated and visually examined under a light microscope and SEM (Fig. 9.), before subjecting to dissolution studies and determining reservoir hardness (N), plus mean drug content per LYO. Characteristics of each LYO are presented in Table 3.

3.5. In vitro delivery of RDN and ALN from formulated MAPs

In vitro delivery of the two compounds from formulated D-MAPs and HF-MAPs, across dermatomed neonatal porcine skin, over 24 h, was investigated, with the use of a Franz cell set up. RDN samples were analysed using HPLC-UV, and ALN samples were derivatised and analysed using a fluorescent microplate reader, as discussed in Sections 2.2 and 3.1. 'Blank' samples of receiver compartment media, throughout the course of the experiment, were also derivatised accordingly, and detected using a microplate reader, to determine fluorescence intensity, which was subsequently subtracted from ALN samples, providing more accurate, ALN-specific readings.

Over the course of 24 h, the cumulative permeation i.e., across porcine skin and into the Franz cell receiver compartment, of RDN, from formulated D-MAPs, was calculated at 4.21 ± 0.65 mg (60.2 ± 9.3 %) (Fig. 10). Similarly, at 24 h, a cumulative amount of 3.19 ± 0.9 mg (59.6 ± 17.1 %) ALN permeated across the skin membrane and into the receiver compartment. Polymer residue was present on the skin surface, at the end of the experiment. This may account for the remainder of each drug loaded into the entirety of the MAP, rather than just the needles.

Both HF-MAP formulations were also subjected to *in vitro* permeation studies with each of the drug-loaded LYO reservoirs. Fig. 11. shows light microscope images of intact swollen HF-MAPs, removed after 24 h of the *in vitro* permeation studies, as well as the surface of the dermatomed skin membrane. Results of these studies are presented in Fig. 12. Cumulative RDN permeation from formulated LYOs, in combination with PVA/PVP MAPs, was calculated at 20.73 ± 1.84 mg, at the end of 24 h, equating to a mean 87.5 % RDN permeation. RDN LYOs in combination with Gantrez® MAPs, allowed for a cumulative permeation of 11.78 ± 3.29 mg RDN (54.1 %), over 24 h. Statistical analysis of these results, by means of an unpaired *t*-test revealed a significant difference in RDN permeation between the two hydrogel formulations ($p = 0.0475$). Similarly, ALN LYOs, in combination with PVA/PVP MAPs, allowed for higher cumulative permeation of the compound, over 24 h. Specifically, PVA/PVP MAPs with ALN LYOs, delivered 4.50 ± 0.86 mg (a mean 50.9 % permeation), *versus* 2.44 ± 0.96 mg with Gantrez® MAPs (mean 25.87 %). Statistical analysis of ALN results, however, by means of an unpaired *t*-test, revealed no significant differences in permeation between the two HF-MAPs ($p = 0.0847$). Best performing HF-MAPs, in this case, PVA/PVP, were thus chosen for further investigation *in vivo*, for both RDN and ALN, in combination with formulated LYO reservoirs.

Table 3
Summary of lyophilised wafer (LYO) reservoir characteristics: thickness (mm), diameter (mm), dissolution time, hardness and drug content; (Means ± S.D., n = 3).

LYO formulation	Reservoir characteristics				
	Thickness (mm)	Diameter (mm)	Dissolution time (min)	Reservoir hardness (N)	Drug content (mg)
RDN LYO	2.51 ± 0.02	12.42 ± 0.03	2.6 ± 0.17	35.6 ± 2.3	23.72 ± 1.79
ALN LYO	2.51 ± 0.02	12.43 ± 0.02	4.5 ± 0.5	36.3 ± 1.5	9.44 ± 0.61

3.6. In vivo delivery of RDN and ALN from formulated MAPs

Formulated MAPs were applied to clean, hair-less areas on the backs of rats, as described in detail in Section 2.7, once a week, for 8 weeks in total. The choice of oral administration of BPs was based on marketed oral treatments for osteoporosis, and was used as a 'treatment control'. Throughout the study, dissolution of D-MAPs and swelling of HF-MAPs, was apparent upon visual inspection of the application sites, when MAPs were removed, confirming successful application of the MAPs. Rats were closely monitored for signs of Grimace throughout the treatment period, were eating and drinking as normal, and alert at all times. At the end of the 8-week treatment period, rats were culled and tissues of interest collected, treated and stored accordingly, as described in Section 2.7.6 for further analysis.

3.6.1. Assessment of treatment efficacy

3.6.1.1. Alkaline phosphatase (ALP) measurements using an enzyme-linked immunosorbent assay (ELISA). Serum and bone ALP levels are important biomarkers in the diagnosis and/or severity assessment of metabolic bone diseases, such as osteoporosis (Tariq et al., 2019). Increased levels of ALP are associated with increased bone loss and the development of osteoporosis, due to a change in the bone remodelling process. ELISA kits were used to determine ALP levels in rat serum and tibia samples, as illustrated in Fig. 13. below.

Mean serum and bone ALP levels were higher in OVX rats (1.97 ± 0.56 ng/mL and 1.40 ± 0.26 ng/mL respectively) compared to healthy SHAM rats (0.77 ± 0.15 ng/mL and 0.94 ± 0.11 ng/mL respectively), as expected and reported before (Yoon et al., 2012). It is important to note that bone ALP in this case, refers to ALP trapped within tibiae samples, whilst bone ALP calculated as part of diagnostic testing in humans, involves the specific detection of the bone ALP isoform in serum samples. Overall, both ORAL and MAP treatment groups caused a reduction in ALP levels in both serum and bone samples, indicating a change in the bone remodelling process, as a result of BP administration. Overall mean ALP levels in MAP groups in serum were 1.23 ± 0.58 ng/mL HF ALN, 1.15 ± 0.45 ng/mL HF RDN, 1.57 ± 0.66 ng/mL D ALN and 1.44 ± 0.25 ng/mL D RDN, all of which were lower than OVX controls. Similarly, mean ALP levels in tibiae samples across MAP groups were 0.70 ± 0.211 ng/mL HF ALN, 0.81 ± 0.213 ng/mL HF RDN, 0.83 ± 0.23 ng/mL D ALN and 1.05 ± 0.27 ng/mL D RDN. Fig. 13. shows the variability in ALP levels across each rat cohort and overall decreasing trends, with some values overlapping with those of SHAM rats, signifying a change towards normal healthy processes. A higher mean ALP level reduction is observed in HF-MAP rats, compared to D-MAPs, in both serum and bone samples, quite possibly due to higher doses of both drugs binding and/or penetrating into bone and causing a more apparent change in the remodelling process. Even though statistical analysis was not possible, due to small sample sizes, multiple parameters and risk of bias, these results, overall, indicate a promising change in bone mineralisation, altering disease progression and normalising the remodelling process to a healthy state. Goes et al. (2012), investigated the effect of alendronate

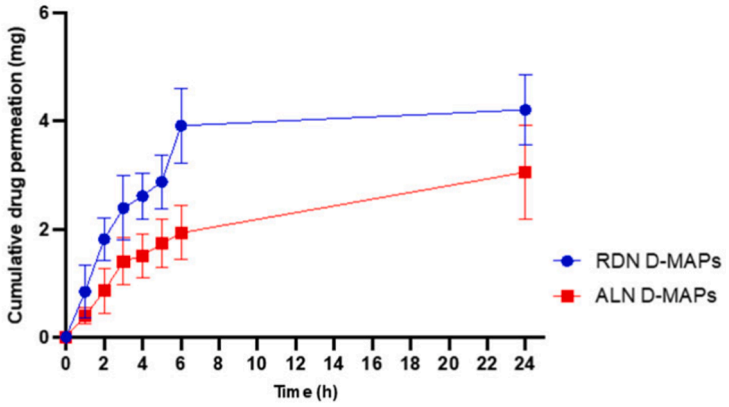

Fig. 10. *In vitro* permeation profiles (mg) of risedronate sodium (RDN) and alendronic acid (ALN)-loaded dissolving microarray patches (D-MAPS), separately, across dermatomed neonatal porcine skin, over 24 h (Means ± S.D., n = 5).

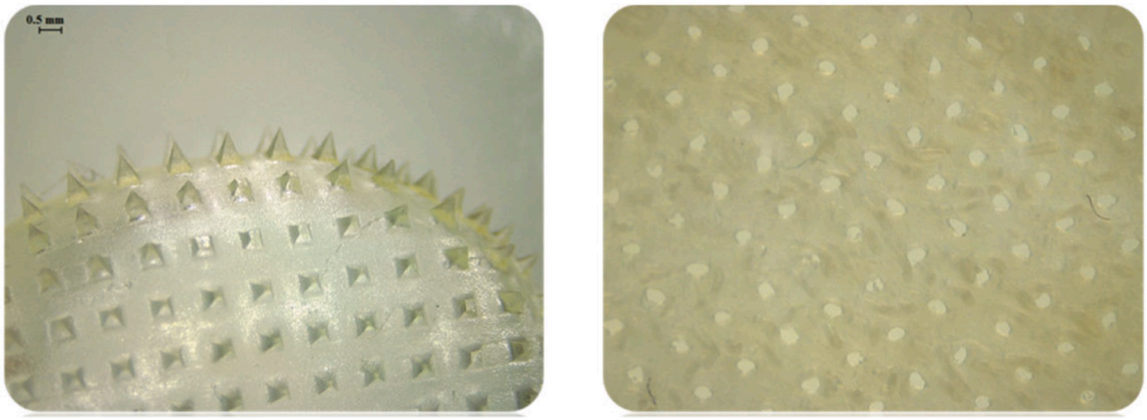

Fig. 11. Light microscope images of **(A)** intact swollen hydrogel-forming microarray patches (HF-MAPs) and **(B)** dermatomed neonatal porcine skin surface, at 24 h of an *in vitro* permeation study.

sodium on both serum and bone-specific rat ALP, in periodontitis, who concluded a significant reduction in both isoforms of the enzyme, in line with observations in the present study. Similarly, risedronate/zinc-hydroxyapatite nanoparticles were delivered to osteoporotic rats, and upon analysis of both serum and bone-specific ALP levels, a significant reduction was observed in treatment groups (Khajuria et al., 2016).

3.6.1.2. Scanning electron microscope (SEM) and energy dispersive X-ray spectroscopy (EDS) analysis of right femur. Fig. 14 shows SEM images of the trabecular mesh on the inside of the distal femur, above (epiphysis) and below (metaphysis) the growth plate in 'SHAM' and 'OVX' rat cohorts. Differences can be seen between SHAM and OVX samples in the trabecular mesh of both the epiphysis and metaphysis of the inside of the distal femur. With regards to trabecular bone on the inside of the metaphysis, in particular (Fig. 14**. B** and **D**), a well-developed, structurally intact trabecular mesh can be seen in the SHAM sample, clearly absent in the OVX one.

Trabecular bone morphology on the inside of the distal epiphysis and metaphysis of femur samples corresponding to each treatment cohort, is presented in Figs. 15 and 16**.**, respectively. Larger pores in the trabecular mesh of epiphyses of ORAL ALN and ORAL RDN samples, can be seen, in comparison to all 4 MAP cohorts. With regards to the distal metaphyses of femurs obtained from treatment groups, in comparison to OVX controls, a marked increase in trabecular network throughout the region is observed. Trabecular mesh does not appear to be fully restored, as is the case in healthy SHAM samples, but a marked improvement in extent of trabecular bone can be seen, relative to OVX control bones, owing to a change in the bone mineralisation and remodelling processes, as a result of BP administration.

Following visual inspection of femur slices, samples coated in carbon, were subjected to EDS analysis, to determine Ca/P ratio within certain regions of the femur. Bones are primarily composed of calcium and phosphorus, and the Ca/P ratio is of particular interest when assessing healthy *versus* diseased states. Interestingly, the diagnosis and management of bone diseases such as osteoporosis is often associated with mass loss, neglecting investigations into elemental composition of bone mineral and subsequent bone quality (Kourkoumelis et al., 2012). The ratio of the two elements in healthy bone should be approximately 2:1, and any deviations from this, especially lower ratios, indicate bone loss (Loughrill et al., 2017). Distal epiphysis, metaphysis and cross-sections of the diaphysis of femur samples were examined and results of EDS analysis are presented in Fig. 17**.**

Mean Ca/P ratios across all cohorts, in selected bone regions, were approximately 2:1, even in OVX control samples. OVX has been reported to affect bone in different ways and not necessarily in a uniform manner even within the same bone type (Francisco et al., 2011; Yousefzadeh et al., 2020). The most apparent difference in Ca/P ratios, was observed in the distal metaphysis (Fig. 17**. B**), with a notable decrease in mean ratio of OVX rats compared to SHAM rats (1.70 ± 0.53 *versus* 2.2 ± 0.07, respectively). Visual examination of this region, under the SEM, described previously, also revealed a difference in trabecular structure between SHAM and OVX rats. Consequently, a general increase in mean Ca/P ratio, in this region of interest, is apparent, across all treatment groups. Changes in Ca/P ratio indicate a change in the bone mineralisation and remodelling processes and a marked restoration of the trabecular network, as observed previously in SEM images. It is apparent

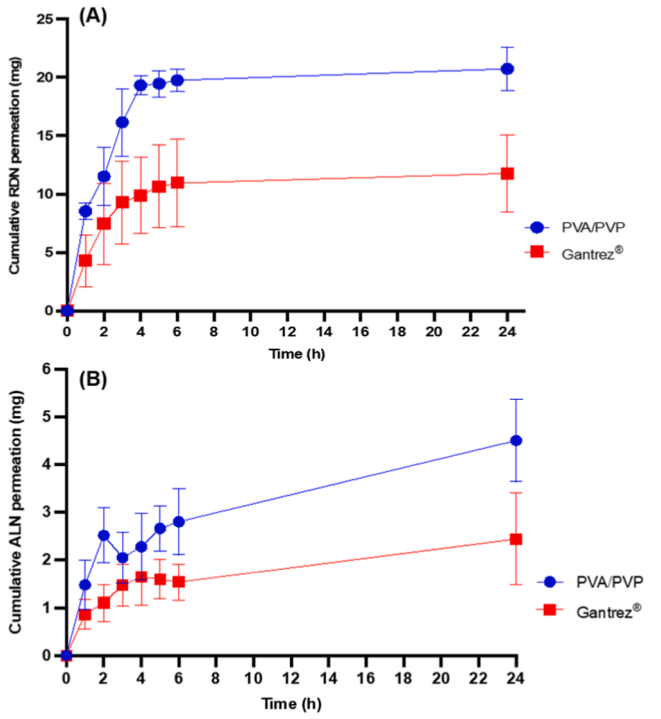

Fig. 12. *In vitro* permeation profiles (mg) of **(A)** risedronate sodium lyophilised wafer reservoirs and **(B)** alendronic acid lyophilised wafer (LYO) reservoirs, in combination with PVA/PVP and Gantrez® hydrogel-forming microarray patches (HF-MAPs), separately, across dermatomed neonatal porcine skin over 24 h; (Means ± S.D., n = 5).

that Ca/P ratio is not uniformly distributed across bone tissue, and regions susceptible to shifts in elemental ratios, could be utilised for future monitoring of disease and/or disease progression, as suggested previously (Kourkoumelis et al., 2012). SEM-EDS analysis has been proven to be a suitable and valuable method of analysing chemical composition in animal bone tissue, both from healthy and diseased animals, in a time and cost-effective manner and could be used more readily in similar types of studies going forwards (Kourkoumelis et al., 2012; Sotiropoulou et al., 2015). Although statistical analysis was not performed on EDS data, overall trends show an increase in mean Ca/P ratios, across all treatment groups, and MAP groups in particular, indicating healthy changes in bone remodelling.

3.6.1.3. Microcomputed tomography (MicroCT/μCT) analysis of left femur. Left femurs retrieved from all rats involved in the study (n = 42) were analysed using MicoCT, as described in Section 2.7.6.4. Femurs are the most commonly investigated bones in studies involving an OVX rat model, and the trabecular region, is of particular interest, as it responds rapidly to intervention and is recommended for osteoporosis research (Yousefzadeh et al., 2020). The femur is additionally one of the main fracture sites in humans and is clinically relevant, so was considered the most appropriate bone sample to examine at the end of the 8-week treatment period (Francisco et al., 2011). Effects of OVX and subsequent treatment can vary between different bone sites, and so differences in microarchitecture are expected to vary across different regions, due to differences in metabolic activity and/or BP binding and penetration into bone (Francisco et al., 2011; Yousefzadeh et al., 2020).

Trabecular bone microarchitecture is a key component of bone quality and strength and is thus extremely important in osteoporosis research (Dempster, 2000). Main parameters defining microarchitecture are trabecular thickness, i.e. the mean thickness of trabeculae in the region of interest, trabecular separation, i.e., the mean distance between borders of segmented trabeculae and trabecular number, i.e., the mean number of trabeculae (Klintström et al., 2014). Additionally, bone volume (BV/TV) (%) refers to the percentage volume of bone compared to the total tissue volume in the region of interest. Porosity (%) is another important factor to consider, especially in disease states such as osteoporosis, where ultimately, treatment aims to reduce bone porosity,

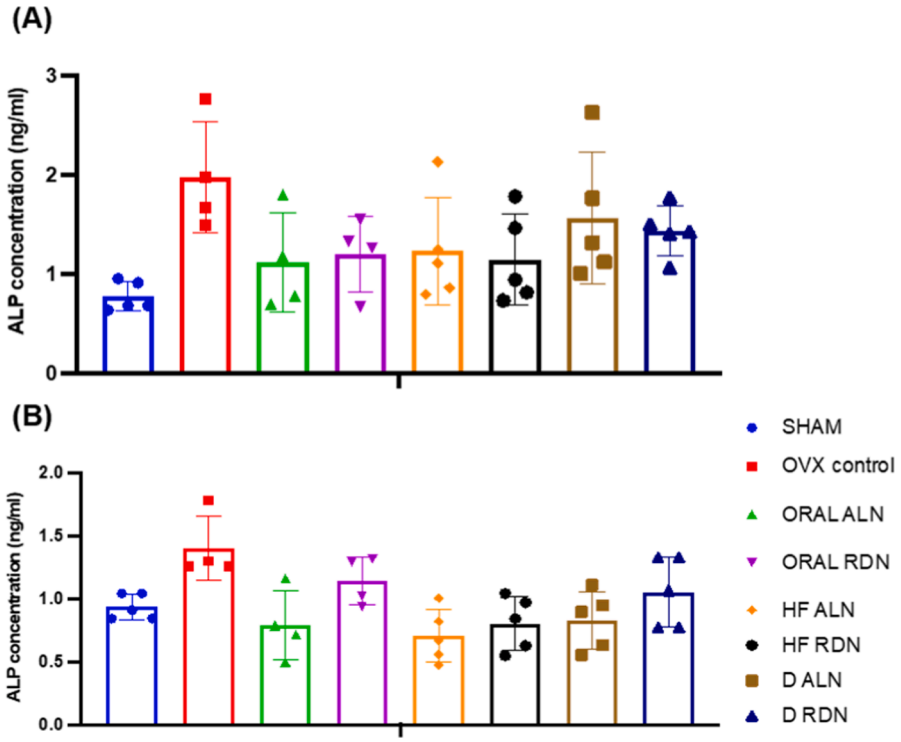

Fig. 13. Alkaline phosphatase levels across all rat cohorts measured in **(A)** serum and **(B)** tibiae samples; (Means ± S.D., n = 4 OVX control, ORAL ALN and ORAL RDN, n = 5 SHAM, and MAP groups).

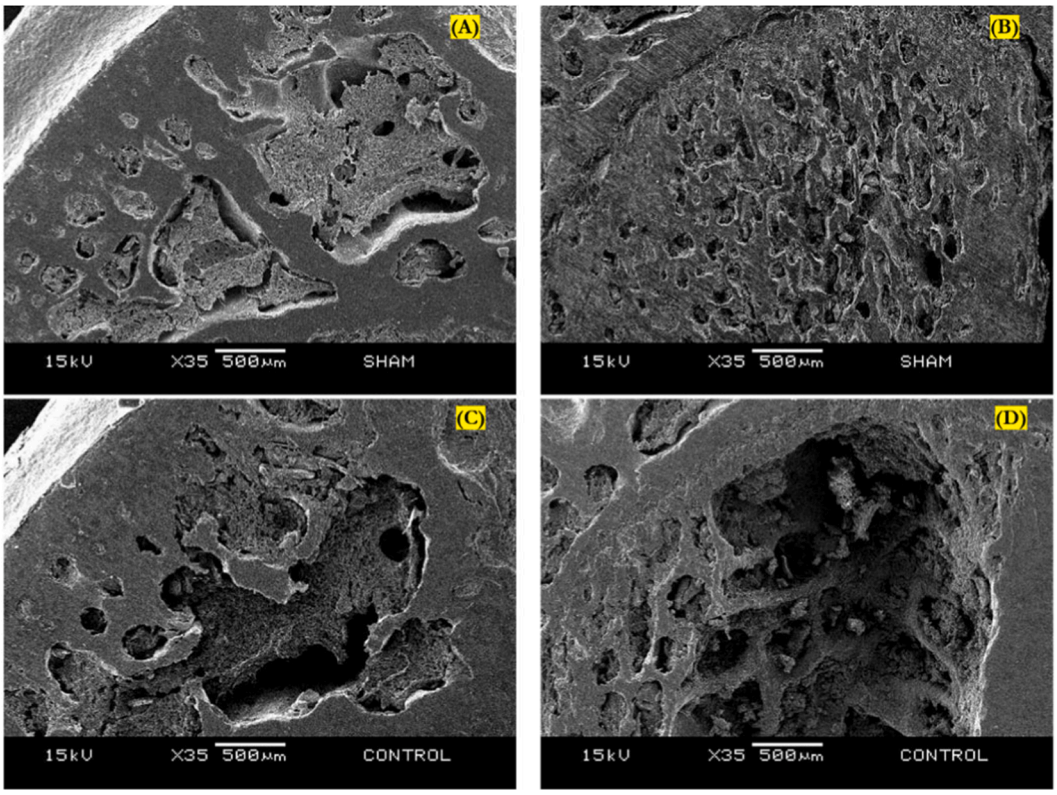

Fig. 14. Scanning electron microscope (SEM) images of **(A-B)** SHAM *versus* **(C-D)** OVX control epiphysis and metaphysis.

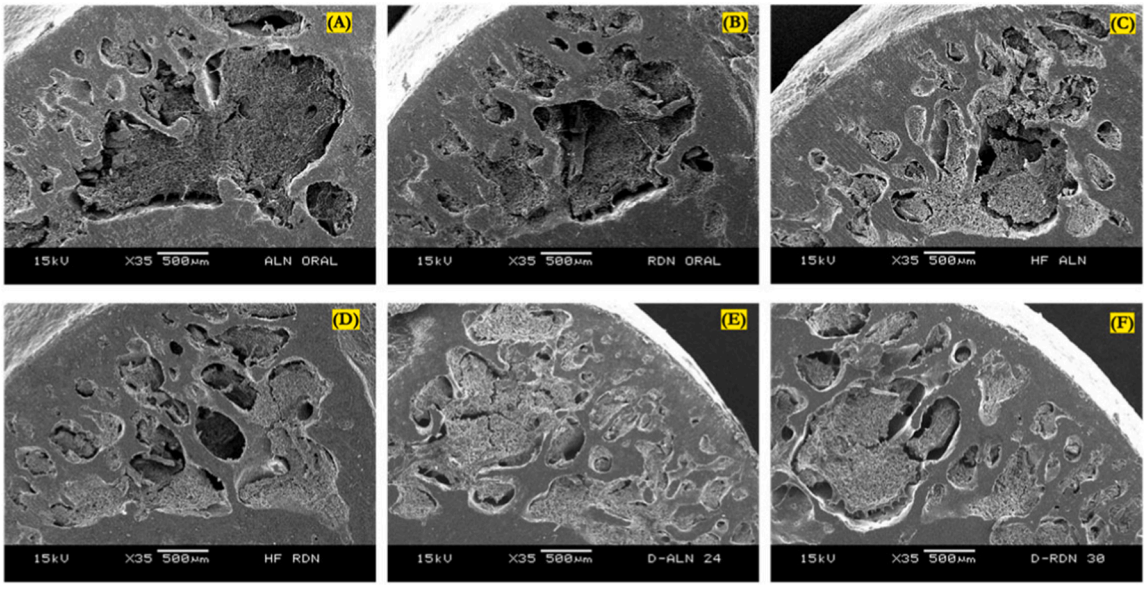

Fig. 15. Scanning electron microscope (SEM) images of distal epiphysis in all six treatment cohorts; **(A)** ORAL ALN, **(B)** ORAL RDN, **(C)** HF-ALN, **(D)** HF-RDN, **(E)** D-ALN, and **(F)** D-RDN.

leading to higher densities and resistance to fractures. In the present study, the distal epiphysis and metaphysis of femur samples obtained from all rat cohorts, were examined. Fig. 18. presents results of the examination of the distal epiphysis of femur samples across all rat cohorts, with regards to each of the bone microarchitecture parameters referred to previously.

OVX causes an increase in bone porosity and decrease in bone volume, a decrease in trabecular thickness and number, and an increase in trabecular separation. Mean SHAM bone volume, in the distal epiphysis, was 58.2 ± 0.54 % and porosity was 41.7 ± 0.54 %, compared to a bone volume of 46.5 ± 1.56 % and 53.4 ± 1.56 % porosity in OVX rats. Overall trends across all 6 treatment groups show marked increases in bone volume, with little variability between each cohort's samples, and a decrease in porosity. Statistical comparison of the mean bone volume of each MAP group *versus* the OVX control was carried out by means of a non-parametric Mann-Whitney test. Significant differences in bone volume were observed between each MAP group and the OVX control ($p < 0.05$). ORAL groups were also compared to OVX controls, separately,

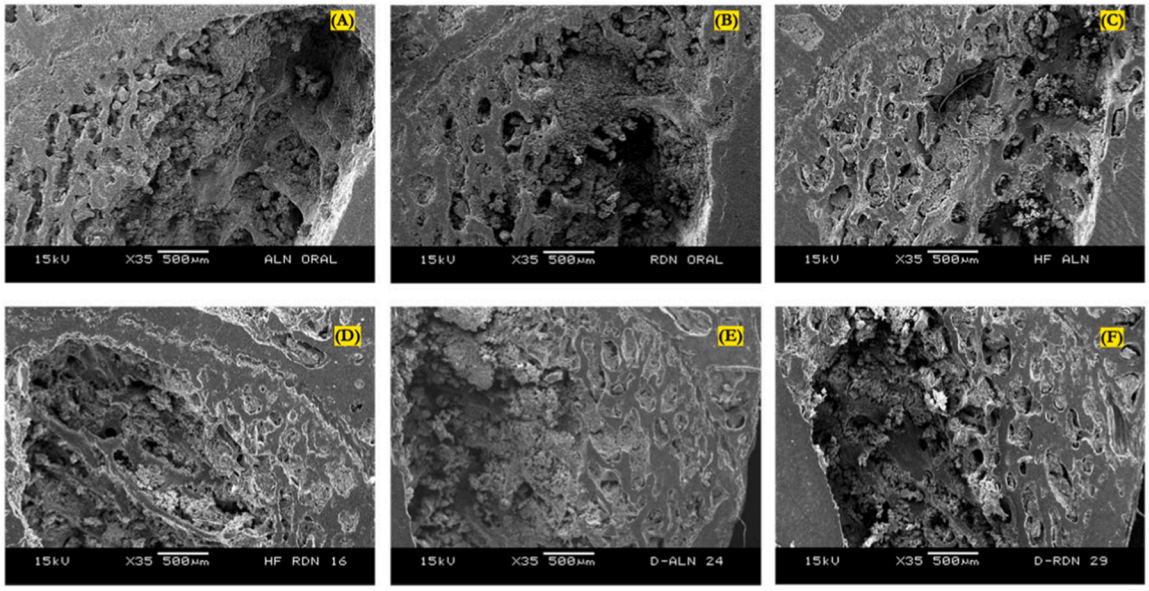

Fig. 16. Scanning electron microscope (SEM) images of distal metaphysis in all six treatment cohorts; **(A)** ORAL ALN, **(B)** ORAL RDN, **(C)** HF-ALN, **(D)** HF-RDN, **(E)** D-ALN, and **(F)** D-RDN.

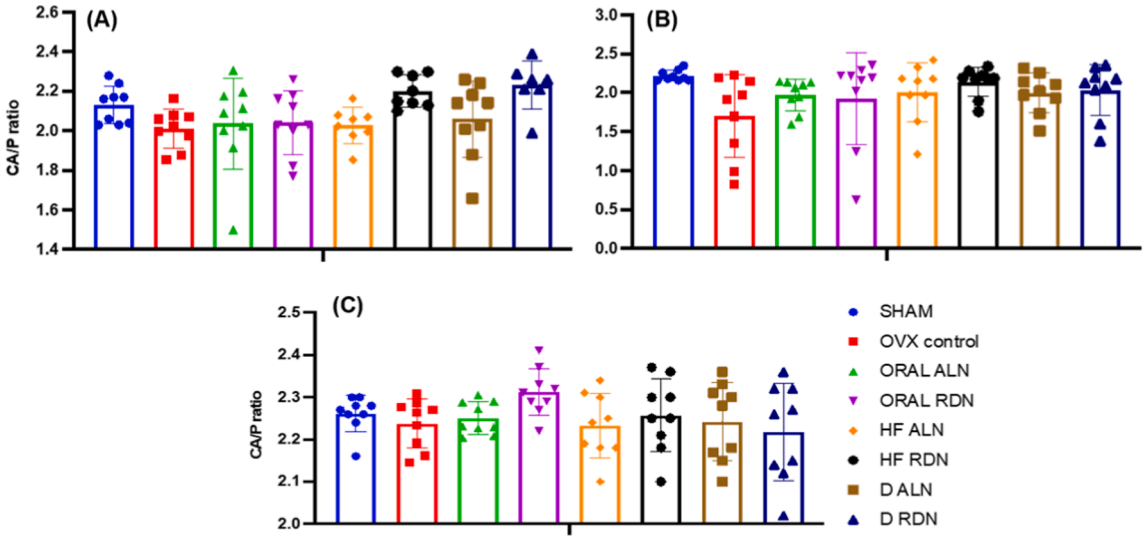

Fig. 17. Calcium/Phosphorus (Ca/P) ratios in regions of interest across all rat cohorts, determined by energy dispersive analysis (EDS); **(A)** distal epiphysis, **(B)** distal metaphysis and **(C)** diaphysis cross-section; (Means ± S.D., n = 3).

and no significant differences were noted, indicating a more pronounced effect on bone parameters, from MAP treatments, rather than ORAL ones. Interestingly, when comparing bone volume of each ALN MAP group to the ORAL ALN cohort, and RDN MAP group to the ORAL RDN group, no significant differences were noted, indicating similar efficacy of the MAP system to the control oral treatments, based on approved clinical doses for osteoporosis. Additionally, comparison of the effects of the HF-MAP and D-MAP design of each drug, separately, also revealed no significant differences. In terms of porosity, comparison of individual pairs of interest, as performed for bone volume data, also revealed significant differences in porosity of all MAP cohorts relative to the OVX control ($p < 0.05$), with no significant differences between ORAL groups and OVX rats.

Increasing trends in trabecular thickness are observed across all treatment cohorts, relative to OVX rats, with individual values overlapping with those of healthy SHAM rats. In terms of statistical comparison of treatment groups and OVX rats, individually, all MAP groups, plus the ORAL RDN group, showed significant increases in trabecular thickness ($p < 0.05$), relative to OVX. An increase in trabecular thickness signifies a change in bone density and subsequent strength and resistance to fracture, highlighting the therapeutic efficacy of all 4 MAP groups. Slight decreasing trends in trabecular separation and increasing trends in trabecular number can also be observed, across MAP treatment groups, however not as distinct as other parameters, and not deemed statistically significant ($p > 0.05$). Overlapping of individual values in MAP groups, with those of healthy SHAM rats, does however indicate a shift in bone microarchitecture towards a healthy state.

Fig. 19 presents results of the examination of the distal metaphysis of femur samples across all rat cohorts, with regards to each of the bone microarchitecture parameters referred to previously. Distinct differences in trabecular bone morphology were observed upon visual examination of this region, under the SEM, further confirmed by a difference in Ca/P ratios.

MicroCT analysis of distal metaphyses of femur samples, showed

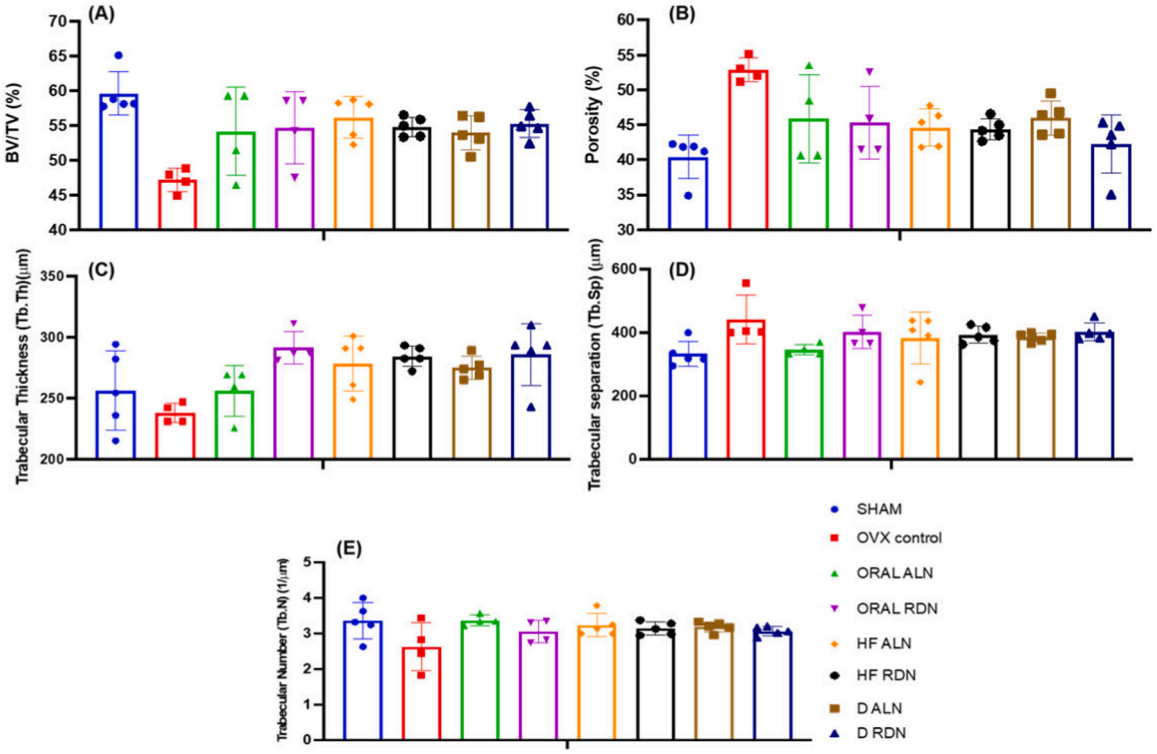

Fig. 18. Comparative evaluation of bone parameters, measured at distal epiphysis region of the left femur, between SHAM, OVX and treatment groups; **(A)** Bone Volume, **(B)** Bone Porosity, **(C)** Trabecular thickness, **(D)** Trabecular separation and **(E)** Trabecular number; (Means ± SD, n = 4 OVX control and ORAL groups, n = 5 for SHAM and MAP groups).

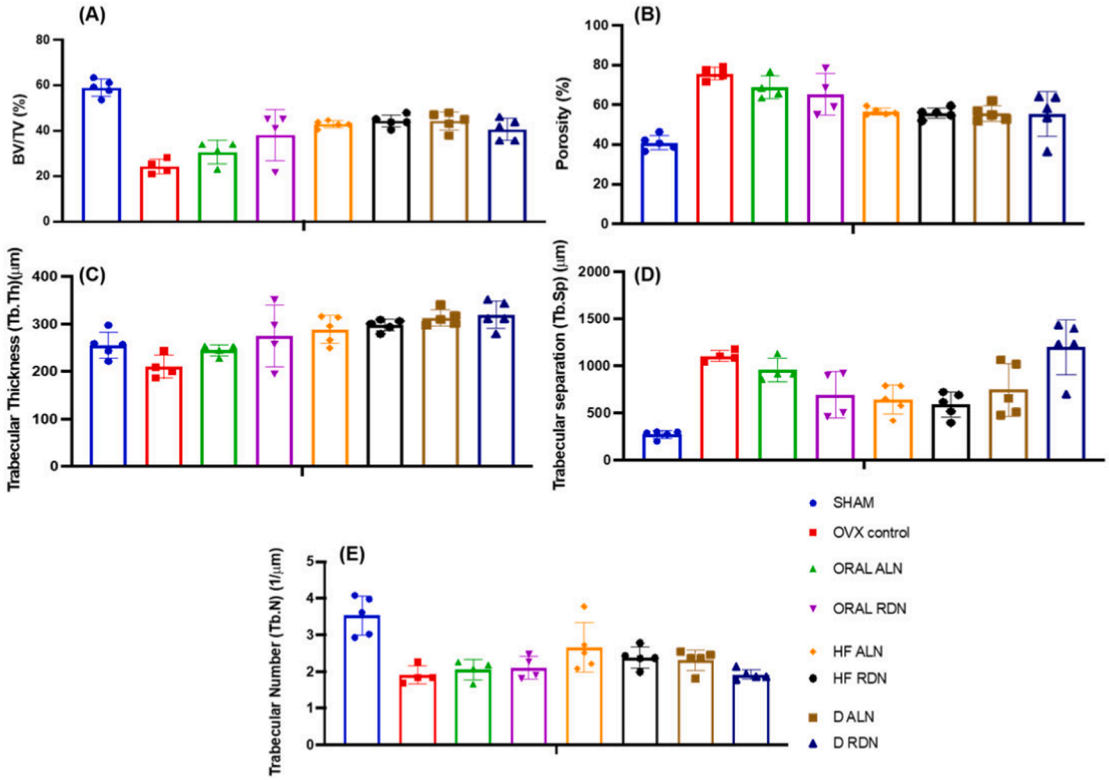

Fig. 19. Comparative evaluation of bone parameters, measured at distal metaphysis region of the left femur, between SHAM, OVX control and treatment groups; **(A)** Bone Volume, **(B)** Bone Porosity, **(C)** Trabecular thickness, **(D)** Trabecular separation and **(E)** Trabecular number; (Means ± SD, n = 4 OVX control and ORAL groups, n = 5 for SHAM and MAP groups).

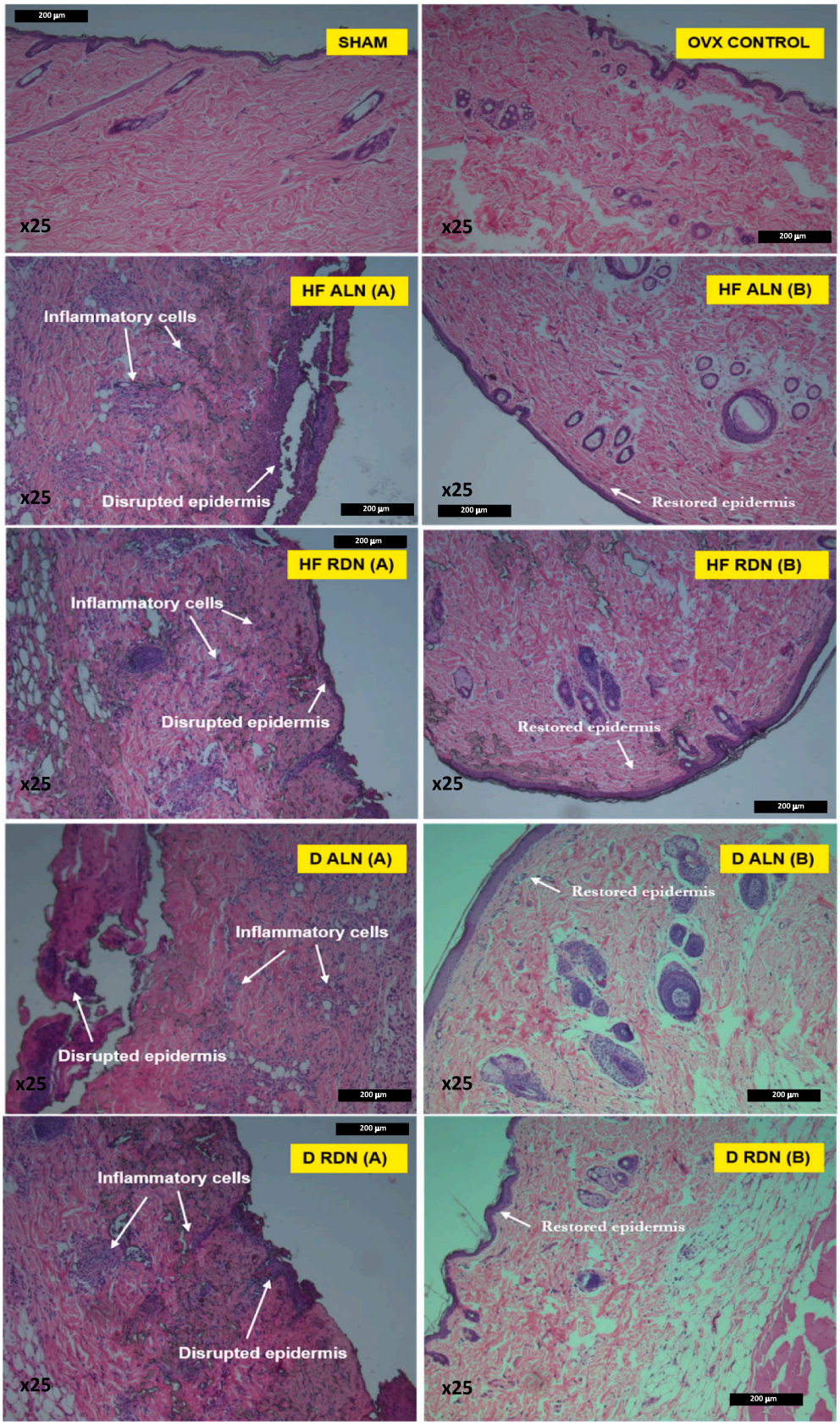

Fig. 20. Annotated histological slides SHAM and OVX control skin samples, as well as **(A)** regions of active inflammation for each MAP cohort, and **(B)** skin restoration post application, for each cohort.

similar overall trends to those of the epiphysis. Bone volume in SHAM rats was calculated at 59.3 ± 5.14 % and porosity at 40.7 ± 5.1 %, which were similar to values obtained in the distal epiphysis. As expected, mean OVX bone volume was significantly lower (22.97 ± 2.17 %) and bone porosity higher (77.02 ± 2.17 %) than SHAM rats ($p = 0.0159$). Bone volume and porosity in the distal metaphysis of OVX rats, were also different to values obtained in the distal epiphysis. A lower bone volume and higher porosity in this region, corresponds to the visual examination and Ca/P ratio estimation of the region. OVX effects on bones, are not uniform across all bone sites, which seems to be the case between the epiphysis and metaphysis, in OVX control rats in this study (Francisco et al., 2011; Yousefzadeh et al., 2020). Kishi et al. (1998) administered human parathyroid hormone to OVX rats, in a similar study to the one discussed in this work, and also reported the distal metaphysis of femur samples to show the most sensitive bone response, compared to other regions of the femur and tibia.

Increasing trends in terms of bone volume and decreasing trends in terms of porosity can be seen across all 6 treatment groups, in Fig. 19**(A)** and **(B)**, with MAP groups having a slightly more pronounced effect on these parameters, compared to ORAL treatments. Statistical comparison of each MAP group with the OVX control, using a non-parametric Mann Whitney test, revealed significant differences in both bone volume and bone porosity ($p < 0.05$). Interestingly, comparison of each MAP group with corresponding ORAL treatments revealed significant differences in ALN loaded MAPs compared to ORAL ALN, with regards to both bone volume and porosity changes, signifying their enhanced effect on bone parameters, relative to control ORAL treatments.

In terms of the other three parameters, decreases in separation and increases in thickness and number, across all treatment groups, are observed. All 4 MAP groups caused significant increases in trabecular thickness, relative to the OVX controls ($p < 0.05$), and interestingly, producing mean values that overlap and in some cases surpass the healthy SHAM values. Due to the high metabolic activity of this region of trabecular bone, microarchitecture changes are more pronounced. In terms of trabecular separation, D-RDN was the only MAP group to not cause a significant change to this parameter relative to the OVX control. The two drugs and two types of MAPs can have different effects on all of these parameters across different trabecular sites, owing to their specific mechanism of action, and so, this different trend seen in this particular treatment cohort, may be attributed to that. Lastly, in terms of trabecular number, increasing trends are seen across all treatment groups, however, not as pronounced as other parameters. Statistical comparison of each treatment group with the OVX control, using a Mann-Whitney test, confirmed no significant changes in trabecular number. Had the treatment period lasted longer, an increase in number of trabeculae, as a result of inhibiting bone resorption, may have been more apparent, especially in the metaphysis region.

Overall, a notable improvement in all five bone parameters is observed across all MAP groups, compared to the OVX rats, in both regions investigated. The 4 MAP groups have shown similar trends to healthy SHAM rats, with more pronounced changes than the control ORAL cohorts. ORAL cohorts were treated with rat equivalent doses of approved clinical human doses, known to manage the disease and thus expected to be efficacious. The observation of more pronounced effects on each bone parameter, as a result of MAP, relative to ORAL treatment, is significant in establishing the therapeutic efficacy of this novel transdermal delivery system. Moreover, there is less variability between MAP samples, compared to ORAL ones. These findings strongly support the potential of MAPs in managing bone loss and shifting the remodelling process back towards a healthy state, thus ultimately, managing osteoporosis Interestingly, trends across all parameters investigated, and across all regions of interest, between HF-MAPs and D-MAPs, are very similar, as indicated by statistical comparisons of the two forms of MAPs for each drug showing no significant differences in bone parameter changes.

3.6.1.4. Histological analysis of skin samples. Fig. 20 shows examples of skin samples derived from SHAM and OVX rats, as well as the 4 MAP groups. For each MAP group, regions of irritated skin, post MAP application, were examined, as well as application sites used throughout the 8-week study, which appeared to have healed. Throughout the treatment period, application sites were rotated, so it was important to examine different regions of skin for any possible signs of chronic inflammation. Histological examination of skin samples, revealed active presence of inflammatory cells in the epidermis and dermis of skin samples from MAP cohorts. Visible skin reactions and subsequent presence of inflammatory cells in the dermis of ALN formulations, were slightly more pronounced than those of RDN formulations, and interestingly, ALN has been reported to irritate patients' oesophagus to a greater degree than RDN (Lanza et al., 2000; Lichtenberger et al., 2000; Peters et al., 2001). Examination of other application sites used throughout the study, however, did not show signs of chronic inflammation, but rather, a restoration of the skin's outermost layers.

Skin irritation was observed upon MAP removal, throughout the 8-week treatment period, an adverse effect which has been reported previously, with the use of MAPs or transdermal gels for BP delivery (Gyanewali et al., 2021; Katsumi et al., 2017, 2012). BPs are known for causing irritation and damage to epithelial cells in the oral cavity and along the GI system, however the exact mechanism by which they cause damage, is not fully understood (Lichtenberger et al., 2000). Skin samples from all rat cohorts in this study, were retrieved and prepared accordingly for histological analysis.

When MAPs were removed from rats during the study, leaching of the LYO reservoirs onto the skin surface seemed to irritate the skin, whilst the area of the HF-MAP remained unaffected. Similarly, signs of irritation were present when D-MAPs fully dissolved, and the baseplate residue remained on the surface of the skin, until patch removal. Katsumi et al., (2017) suggested that irritation was significantly limited when incorporating the BP solely into MNs, rather than the whole MAP. This would allow for the compounds to be delivered into the dermis and rapidly taken up the microcirculation, rather than residing on the surface of skin for long periods of time, causing adverse reactions, due to the inherent acidity of BPs. Similarly, a change in the shape and/or size of LYOs preventing leakage of the reservoir onto the surface of skin, may prevent skin reactions observed in this study. In the future, and with the regulation and commercialisation of MAPs in mind, a change in design of both MAP types would be needed, in order to minimise the presence of both compounds on the surface of skin, thus limiting irritation and inflammation at application site.

3.7. Future considerations

When considering this work for future patient use, both MAP types have proven their therapeutic efficacy *in vivo*, and undoubtedly have great potential as an alternative treatment option for patients living with osteoporosis. Effective doses for management of the disease would need to be determined, and based on these, make approximations on final patch size for patient use. Patch and/or reservoir design would also need to be altered to avoid unnecessary spillage of BPs onto the skin surface, thus preventing adverse effects such as irritation, seen earlier in this work. D-MAPs offer a more patient-friendly alternative to oral preparations, due to the ease of self-application as a one-step system, compared to HF-MAPs, involving a two-step application process. Further *in vivo* experimentation would need to take place to explore the pharmacokinetic effects of both drugs when delivered *via* MAPs. Larger animal models may also be used to further explore pharmacodynamic and pharmacokinetic effects of the patches. Finally, with market approval as the end goal for MN technology, parameters such as long-term stability, sterility, content uniformity and packaging, are few of the many factors that need to be taken into consideration in the future development of the MAPs formulated and investigated in this work.

4. Conclusion

RDN and ALN were formulated into D-MAPs, and LYO reservoirs to be used in combination with PVA/PVP HF-MAPs, characterised accordingly and then subjected to *in vitro* permeation studies. Formulated MAPs were further investigated, in terms of therapeutic efficacy, *in vivo*, using an osteoporotic female Sprague Dawley rat model. Weekly treatment with BP-loaded MAPs and control ORAL preparations was initiated 3 months post-ovariectomy, and continued for 8 weeks. Formulated MAPs proved their therapeutic efficacy, by decreasing serum and bone ALP levels, increasing Ca/P ratios and altering bone microarchitecture parameters towards a healthy state. In most cases, MAPs caused more pronounced, statistically significant effects on bone parameters, compared to control ORAL treatments, thus further confirming their efficacy and potential as a treatment option for patients living with osteoporosis. Further development and adjustment of patch design and drug loading may overcome adverse effects of irritation and inflammation observed on the skin surface. Moreover, pharmacokinetic analyses of MAP-mediated drug delivery could be investigated, in order to compare blood concentration profiles of the oral *versus* transdermal routes of delivery. This study showed that MN technology, has the potential to be utilised as a novel, patient-friendly, alternative treatment option, in the weekly management of osteoporosis.

Funding sources

This work was supported by the Queen's University Belfast Agility Fund and the Department for the Economy Northern Ireland PhD studentship.

CRediT authorship contribution statement

Anastasia Ripolin: Writing – review & editing, Writing – original draft, Visualization, Validation, Project administration, Investigation, Formal analysis, Data curation, Conceptualization. **Fabiana Volpe-Zanutto:** Project administration, Investigation, Conceptualization. **Akmal H. Sabri:** Investigation. **Victor Augusto Benedicto dos Santos:** . **Sidney R. Figueroba:** Investigation. **Arthur A.C. Bezerra:** Investigation. **Brendo Vinicius Rodrigues Louredo:** Investigation. **Pablo Agustin Vargas:** Investigation. **Mary B. McGuckin:** Investigation. **Aaron R.J. Hutton:** Writing – review & editing, Investigation. **Eneko Larrañeta:** Supervision, Project administration, Investigation. **Michelle Franz-Montan:** Supervision, Resources, Project administration, Investigation, Conceptualization. **Ryan F. Donnelly:** Writing – review & editing, Supervision, Resources, Project administration, Methodology, Funding acquisition, Conceptualization.

Declaration of competing interest

The authors declare that they have no known competing financial interests or personal relationships that could have appeared to influence the work reported in this paper.

Data availability

Data will be made available on request.

Acknowledgements

Anastasia Ripolin is a PhD candidate funded by the Department for the Economy (N. Ireland) studentship. We thank technicians Fabio Vinisios Padilha and Adriano Luis Martins for their expertise and support throughout the *in vivo* part of this work. We also thank Fabiane Pohlmann de Athayde for her expertise and help with the histological analysis.

References

Alkilani, A.Z., McCrudden, M.T.C., Donnelly, R.F., 2015. Transdermal drug delivery: Innovative pharmaceutical developments based on disruption of the barrier properties of the stratum corneum. Pharmaceutics 7, 438–470. https://doi.org/10.3390/pharmaceutics7040438.

Anjani, Q.K., Permana, A.D., Cárcamo-Martínez, Á., Domínguez-Robles, J., Tekko, I.A., Larrañeta, E., Vora, L.K., Ramadon, D., Donnelly, R.F., 2021. Versatility of hydrogel-forming microneedles in in vitro transdermal delivery of tuberculosis drugs. Eur. J. Pharm. Biopharm. 158, 294–312. https://doi.org/10.1016/j.ejpb.2020.12.003.

Clynes, M.A., Harvey, N.C., Curtis, E.M., Fuggle, N.R., Dennison, E.M., Cooper, C., 2020. The epidemiology of osteoporosis. Br. Med. Bull. 133, 105–117. https://doi.org/10.1093/bmb/ldaa005.

Cosman, F., de Beur, S.J., LeBoff, M.S., Lewiecki, E.M., Tanner, B., Randall, S., Lindsay, R., 2014. Clinician's Guide to Prevention and Treatment of Osteoporosis. Osteoporos. Int. 25, 2359–2381. https://doi.org/10.1007/s00198-014-2794-2.

Coxon, F.P., Ebetino, F.H., Mules, E.H., Seabra, M.C., McKenna, C.E., Rogers, M.J., 2005. Phosphonocarboxylate inhibitors of Rab geranylgeranyl transferase disrupt the prenylation and membrane localization of Rab proteins in osteoclasts in vitro and in vivo. Bone 37, 349–358. https://doi.org/10.1016/j.bone.2005.04.021.

de Oliveira, M.A., Moraes, R., Castanha, E.B., Prevedello, A.S., Vieira Filho, J., Bussolaro, F.A., García Cava, D., 2022. Osteoporosis Screening: Applied Methods and Technological Trends. Med. Eng. Phys. 108, 103887 https://doi.org/10.1016/j.medengphy.2022.103887.

Dempster, D.W., 2000. The contribution of trabecular architecture to cancellous bone quality. J. Bone Miner. Res. 15, 20–23. https://doi.org/10.1359/jbmr.2000.15.1.20.

Donnelly, R.F., Singh, T.R.R., Garland, M.J., Migalska, K., Majithiya, R., McCrudden, C. M., Kole, P.L., Mahmood, T.M.T., McCarthy, H.O., Woolfson, A.D., 2012. Hydrogel-forming microneedle arrays for enhanced transdermal drug delivery. Adv. Funct. Mater. 22, 4879–4890. https://doi.org/10.1002/adfm.201200864.

Donnelly, R.F., McCrudden, M.T.C., Alkilani, A.Z., Larrañeta, E., McAlister, E., Courtenay, A.J., Kearney, M.C., Raj Singh, T.R., McCarthy, H.O., Kett, V.L., Caffarel-Salvador, E., Al-Zahrani, S., Woolfson, A.D., 2014a. Hydrogel-forming microneedles prepared from "super swelling" polymers combined with lyophilised wafers for transdermal drug delivery. PLoS One 9. https://doi.org/10.1371/journal.pone.0111547.

Donnelly, R.F., Mooney, K., McCrudden, M.T.C., Vicente-Pérez, E.M., Belaid, L., González-Vázquez, P., McElnay, J.C., Woolfson, A.D., 2014b. Hydrogel-forming microneedles increase in volume during swelling in skin, but skin barrier function recovery is unaffected. J. Pharm. Sci. 103, 1478–1486. https://doi.org/10.1002/jps.23921.

Figueroba, S.R., Moreira, J.C., Amorim, K.S., Cunha, L.D.L.L., Morais, T.M.L., Ferreira, L. E.N., Groppo, F.C., 2021. Effect of glucosamine sulphate on the temporomandibular joint of ovariectomised rats. Br. J. Oral Maxillofac. Surg. 59, 202–208. https://doi.org/10.1016/j.bjoms.2020.08.078.

Francisco, J.I., Yu, Y., Oliver, R.A., Walsh, W.R., 2011. Relationship between age, skeletal site, and time post-ovariectomy on bone mineral and trabecular microarchitecture in rats. J. Orthop. Res. 29, 189–196. https://doi.org/10.1002/jor.21217.

Garland, M.J., Singh, T.R.R., Woolfson, A.D., Donnelly, R.F., 2011. Electrically enhanced solute permeation across poly(ethylene glycol)-crosslinked poly(methyl vinyl ether-co-maleic acid) hydrogels: Effect of hydrogel crosslink density and ionic conductivity. Int. J. Pharm. 406, 91–98. https://doi.org/10.1016/j.ijpharm.2011.01.002.

Goes, P., Melo, I.M., Dutra, C.S., Lima, A.P.S., Lima, V., 2012. Effect of alendronate on bone-specific alkaline phosphatase on periodontal bone loss in rats. Arch. Oral Biol. 57, 1537–1544. https://doi.org/10.1016/j.archoralbio.2012.07.007.

González-Vázquez, P., Larrañeta, E., McCrudden, M.T.C., Jarrahian, C., Rein-Weston, A., Quintanar-Solares, M., Zehrung, D., McCarthy, H., Courtenay, A.J., Donnelly, R.F., 2017. Transdermal delivery of gentamicin using dissolving microneedle arrays for potential treatment of neonatal sepsis. J. Control. Release 265, 30–40. https://doi.org/10.1016/j.jconrel.2017.07.032.

Gyanewali, S., Kesharwani, P., Sheikh, A., Ahmad, F.J., Trivedi, R., Talegaonkar, S., 2021. Formulation development and in vitro–in vivo assessment of protransfersomal gel of anti-resorptive drug in osteoporosis treatment. Int. J. Pharm. 608, 121060 https://doi.org/10.1016/j.ijpharm.2021.121060.

Katsumi, H., Liu, S., Tanaka, Y., Hitomi, K., Hayashi, R., Hirai, Y., Kusamori, K., Quan, Y., Kamiyama, F., Sakane, T., Yamamoto, A., 2012. Development of a Novel Self-Dissolving Microneedle Array of Alendronate, a Nitrogen-Containing Bisphosphonate: Evaluation of Transdermal Absorption, Safety, and Pharmacological Effects After Application in Rats. J. Pharm. Sci. 101, 3230–3238. https://doi.org/10.1002/jps.23136.

Katsumi, H., Tanaka, Y., Hitomi, K., Liu, S., Quan, Y., Kamiyama, F., Sakane, T., Yamamoto, A., 2017. Efficient Transdermal Delivery of Alendronate, a Nitrogen-Containing Bisphosphonate, Using Tip-Loaded Self-Dissolving Microneedle Arrays for the Treatment of Osteoporosis. Pharmaceutics 9, 29. https://doi.org/10.3390/pharmaceutics9030029.

Khajuria, D.K., Disha, C., Vasireddi, R., Razdan, R., Mahapatra, D.R., 2016. Risedronate/zinc-hydroxyapatite based nanomedicine for osteoporosis. Mater. Sci. Eng. C 63, 78–87. https://doi.org/10.1016/j.msec.2016.02.062.

Kishi, T., Hagino, H., Kishimoto, H., Nagashima, H., 1998. Bone responses at various skeletal sites to human parathyroid hormone in ovariectomized rats: Effects of long-term administration, withdrawal, and readministration. Bone 22, 515–522. https://doi.org/10.1016/S8756-3282(98)00045-3.

Klintström, E., Smedby, Klintström, B., Brismar, T.B., Moreno, R., 2014. Trabecular bone histomorphometric measurements and contrast-to-noise ratio in CBCT. Dentomaxillofacial Radiol. 43. DOI: 10.1259/dmfr.20140196.

Kourkoumelis, N., Balatsoukas, I., Tzaphlidou, M., 2012. Ca/P concentration ratio at different sites of normal and osteoporotic rabbit bones evaluated by Auger and energy dispersive X-ray spectroscopy. J. Biol. Phys. 38, 279–291. https://doi.org/10.1007/s10867-011-9247-3.

Kusamori, K., Katsumi, H., Abe, M., Ueda, A., Sakai, R., Hayashi, R., Hirai, Y., Quan, Y.S., Kamiyama, F., Sakane, T., Yamamoto, A., 2010. Development of a novel transdermal patch of alendronate, a nitrogen-containing bisphosphonate, for the treatment of osteoporosis. J. Bone Miner. Res. 25, 2582–2591. https://doi.org/10.1002/jbmr.147.

Lanza, F.L., Hunt, R.H., Thomson, A.B.R., Provenza, J.M., Blank, M.A., 2000. Endoscopic comparison of esophageal and gastroduodenal effects of risedronate and alendronate in postmenopausal women. Gastroenterology 119, 631–638. https://doi.org/10.1053/gast.2000.16517.

Larrañeta, E., Moore, J., Vicente-Pérez, E.M., González-Vázquez, P., Lutton, R., Woolfson, A.D., Donnelly, R.F., 2014. A proposed model membrane and test method for microneedle insertion studies. Int. J. Pharm. 472, 65–73. https://doi.org/10.1016/j.ijpharm.2014.05.042.

Lichtenberger, L.M., Romero, J.J., Gibson, G.W., Blank, M.A., 2000. Effect of bisphosphonates on surface hydrophobicity and phosphatidylcholine concentration of rodent gastric mucosa. Dig. Dis. Sci. 45, 1792–1801. https://doi.org/10.1023/A:1005574009856.

Loughrill, E., Wray, D., Christides, T., Zand, N., 2017. Calcium to phosphorus ratio, essential elements and vitamin D content of infant foods in the UK: Possible implications for bone health. Matern. Child Nutr. 13, 1–10. https://doi.org/10.1111/mcn.12368.

Mirza, F., Canalis, E., 2015. MANAGEMENT OF ENDOCRINE DISEASE: Secondary osteoporosis: pathophysiology and management. Eur. J. Endocrinol. 173, R131–R151. https://doi.org/10.1530/eje-15-0118.

Naito, C., Katsumi, H., Yoneto, K., Omura, M., Nishidono, M., Kamei, S., Mizoguchi, A., Tamba, A., Tanaka, A., Morishita, M., Yamamoto, A., 2019. Development of a phosphoric acid-mediated hyaluronic acid gel sheet for efficient transdermal delivery of alendronate for anti-osteoporotic therapy. Pharmaceutics 11. https://doi.org/10.3390/pharmaceutics11120643.

Peter, C.P., Kindt, M.V., Majka, J.A., 1998. Comparative study of potential for bisphosphonates to damage gastric mucosa of rats. Dig. Dis. Sci. 43, 1009–1015. https://doi.org/10.1023/A:1018826600877.

Peters, M.L., Leonard, M., Licata, A.A., 2001. Role of alendronate and risedronate in preventing and treating osteoporosis. Cleve. Clin. J. Med. 68, 945–951. https://doi.org/10.3949/ccjm.68.11.945.

Ramadon, D., McCrudden, M.T.C., Courtenay, A.J., Donnelly, R.F., 2021. Enhancement strategies for transdermal drug delivery systems: current trends and applications, Drug Delivery and Translational Research. Springer US. DOI: 10.1007/s13346-021-00909-6.

Reagan-Shaw, S., Nihal, M., Ahmad, N., 2008. Dose translation from animal to human studies revisited. FASEB J. 22, 659–661. https://doi.org/10.1096/fj.07-9574lsf.

Sabri, A.H.B., Anjani, Q.K., Utomo, E., Ripolin, A., Donnelly, R.F., 2022. Development and characterization of a dry reservoir-hydrogel-forming microneedles composite for minimally invasive delivery of cefazolin. Int. J. Pharm. 617, 121593 https://doi.org/10.1016/j.ijpharm.2022.121593.

Sengupta, S., Arshad, M., Sharma, S., Dubey, M., Singh, M.M., 2005. Attainment of peak bone mass and bone turnover rate in relation to estrous cycle, pregnancy and lactation in colony-bred Sprague-Dawley rats: Suitability for studies on pathophysiology of bone and therapeutic measures for its management. J. Steroid Biochem. Mol. Biol. 94, 421–429. https://doi.org/10.1016/j.jsbmb.2004.12.039.

Sotiropoulou, P., Fountos, G., Martini, N., Koukou, V., Michail, C., Kandarakis, I., Nikiforidis, G., 2015. Bone calcium/phosphorus ratio determination using dual energy X-ray method. Phys. Medica 31, 307–313. https://doi.org/10.1016/j.ejmp.2015.01.019.

Sozen, T., Ozisik, L., Calik Basaran, N., 2017. An overview and management of osteoporosis. Eur. J. Rheumatol. 4, 46–56. https://doi.org/10.5152/eurjrheum.2016.048.

Sultana, N., Ali, A., Waheed, A., Jabi, B., Yaqub khan, M., Mujeeb, M., Sultana, Y., Aqil, M., 2023. Dissolving microneedle transdermal patch loaded with Risedronate sodium and Ursolic acid bipartite nanotransfersomes to combat osteoporosis: Optimization, characterization, in vitro and ex vivo assessment. Int. J. Pharm. 644, 123335. DOI: 10.1016/j.ijpharm.2023.123335.

Tariq, S., Tariq, S., Lone, K.P., Khaliq, S., 2019. Alkaline phosphatase is a predictor of Bone Mineral Density in postmenopausal females. Pakistan J. Med. Sci. 35, 749–753. https://doi.org/10.12669/pjms.35.3.188.

Tekko, I.A., Chen, G., Domínguez-Robles, J., Thakur, R.R.S., Hamdan, I.M.N., Vora, L., Larrañeta, E., McElnay, J.C., McCarthy, H.O., Rooney, M., Donnelly, R.F., 2020. Development and characterisation of novel poly (vinyl alcohol)/poly (vinyl pyrrolidone)-based hydrogel-forming microneedle arrays for enhanced and sustained transdermal delivery of methotrexate. Int. J. Pharm. 586, 119580 https://doi.org/10.1016/j.ijpharm.2020.119580.

Thompson, D.D., Simmons, H.A., Pirie, C.M., Ke, H.Z., 1995. FDA guidelines and animal models for osteoporosis. Bone 17, 125–133. https://doi.org/10.1016/8756-3282(95)00285-L.

Tuan-Mahmood, T.M., McCrudden, M.T.C., Torrisi, B.M., McAlister, E., Garland, M.J., Singh, T.R.R., Donnelly, R.F., 2013. Microneedles for intradermal and transdermal drug delivery. Eur. J. Pharm. Sci. 50, 623–637. https://doi.org/10.1016/j.ejps.2013.05.005.

Vestergaard, P., Schwartz, K., Pinholt, E.M., Rejnmark, L., Mosekilde, L., 2010. Gastric and esophagus events before and during treatment of osteoporosis. Calcif. Tissue Int. 86, 110–115. https://doi.org/10.1007/s00223-009-9323-x.

Wong, R.S.H., Ashton, M., Dodou, K., 2015. Effect of crosslinking agent concentration on the properties of unmedicated hydrogels. Pharmaceutics 7, 305–319. https://doi.org/10.3390/pharmaceutics7030305.

Wu, Y., Adeeb, S., Doschak, M.R., 2015. Using micro-CT derived bone microarchitecture to analyze bone stiffness - a case study on osteoporosis rat bone. Front. Endocrinol. (lausanne) 6, 1–7. https://doi.org/10.3389/fendo.2015.00080.

Yamamoto, K., Kishino, M., Nakamura, S., Tokushige, K., 2019. Symptoms and upper gastrointestinal mucosal injury associated with bisphosphonate therapy. Intern. Med. 58, 1049–1056. https://doi.org/10.2169/internalmedicine.1271-18.

Yoon, K.H., Cho, D.C., Yu, S.H., Kim, K.T., Jeon, Y., Sung, J.K., 2012. The change of bone metabolism in ovariectomized rats: Analyses of MicroCT scan and biochemical markers of bone turnover. J. Korean Neurosurg. Soc. 51, 323–327. https://doi.org/10.3340/jkns.2012.51.6.323.

Yousefzadeh, N., Kashfi, K., Jeddi, S., Ghasemi, A., Physiology, E., Sciences, B., Education, B., Physiology, E., Street, A., Blvd, D., 2020. Review article : ovariectomised rat model of osteoporosis. EXCLI J. 19, 89–107.

Zhu, J., March, L., 2022. Treating osteoporosis: risks and management. Aust. Prescr. 45, 150–157. https://doi.org/10.18773/austprescr.2022.054.